Supplementary Information

Bifacial tandem solar cells power generation density boost unleashed by high throughput optoelectrical modeling

Jiahong Tang[1], Junfeng Xue[2], Huaiwang Xu[1], Yujing Li[1], Shuping Lin[3,4], Boyan Li[3,4], Dalong Zhong[3,4], Gang Li[5], Yan Jiang[1], Qi Chen[1]**

J.Tang, H. Xu, Y.Li, Y.Jiang, Q.Chen

School of materials science and engineering, Beijing Institute of Technology, Beijing 100081, China

Email: yan.jiang@bit.edu.cn, qic@bit.edu.cn

J.Xue

School of Automation, Beijing Institute of Technology, Beijing 100081, China

S.Lin, B.Li, D.Zhong

National Institute of Clean-and-Low-Carbon Energy, Beijing 102211, China

Beijing Engineering Research Center of Nano-Structure Thin-Film Solar Cell, Beijing 102211, China

G.Li

Department of Electronic and Information Engineering, Research Institute for Smart Energy, The Hong Kong Polytechnic University, Hong Kong 999077, China

Keywords:

Bifacial solar cells, Tandem solar cells, Perovskite, $Cu(In,Ga)Se_2$, Power generation density

1. Optical Simulation

We use the transfer matrix method (TMM) to perform optical simulations of the tandem device stack. TMM assumes that light propagates along the Z-axis and that the layers in the stack are continuous and uniform in the XY-plane. Unlike silicon cells, which have a textured structure, the nanoscale roughness of the surfaces of CIGS and perovskite in this work is neglected, assuming they are flat and smooth. To reduce computational complexity, all materials used in this work are treated as homogeneous. For TMM, abstracting solar cell structure into a stack of uniform one-dimensional materials seems to have a negligible effect[1-3]. Additionally, we must assume that the optical parameters of the materials do not change with variations in factors such as light exposure and temperature. This assumption holds when calculating the power generation potential in real-world conditions. The optical simulation is conducted by the open-source modeling platform EYcalc[4]. This software is composed of 4 sub-modules: a) Irradiance module, b) Optical module, c) Electric module and d) Energy Yield module. The basic methodology is depicted in Figure S1. We call the AM 1.5G spectrum from the irradiance module and the optical stack modeling is established based on the configuration of the state-of-art PVSK/CIGS monofacial tandem solar cell[5, 6]. The optical parameters of the materials, refractive index (n) and extinction coefficient (k), used in this work are summarized in Figure S1 and S2. The comparison of the simulated reflectance and EQE with the experimental results for the monofacial perovskite (PVSK)/Cu(In,Ga)Se (CIGS) tandem solar cell is shown in Figure S3. An optimized configuration is present to boost the optical absorptance of the two sub-cells as shown in Figure S4. The detailed optical stack is illustrated in Figure S5. As for bifacial PVSK/CIGS tandem solar cells, ITO[7] is used to replace the molybdenum as the rear side electrode.

Once the device stack and spectrum are specified, we can obtain the absorption of each layer as a function of wavelengths, and thereby calculate the photogenerated current density following the equation beneath:

$$J_{sc} = q \times \int_0^{\lambda_{E_g}} \frac{\lambda}{hc} EQE(\lambda) \Phi_{Spectrum} d\lambda$$

Where q is the electronic charge, h is the Plank constant, c is the light speed in vacuum, λ is the wavelength and λ_{E_g} is the maximum wavelength that can be absorbed by active layers. The $EQE(\lambda)$ is considered as the $Absorption(\lambda) \times CE$ (the collecting efficiency, represent the ratio that carriers can be collected after photoexcitation). The average CE is set to be 95% for perovskite and 97% for CIGS, respectively. $\Phi_{Spectrum}$ represents the spectral irradiance as a function of wavelength. The AM 1.5G spectrum is applied as the standard test condition.

The introduction of rear side illumination will increase the J_{sc} of CIGS bottom cell, the absorptance spectra and parasitic losses for bifacial PVSK/CIGS cell with front side illumination (Figure S6) and rear side illumination (Figure S7) are depicted. As the bandgap of CIGS is narrower than perovskite, the rear side irradiation cannot be absorbed by the perovskite top cell.

In general, the J_{sc} of bottom sub-cell under 4T configuration is lower than that of 2T counterpart due to the interfacial reflection on the air gap between the top and bottom sub-cells according to the Fresnel Equations. However, we believe the interfacial reflection can be eliminated by replacing the anti-reflection coatings (ARC) and air gap with an encapsulant that possesses a highly matched refractive index to the adjacent TCO layers. The detailed J_{sc} distribution for filtered CIGS sub-cell in 2T and 4T configurations can be seen in Figure S8, where the J_{sc} in individual sub-cells for the two configurations

are of high consistency.

2. Electrical parameters and device performance

Electrically, we use the Shockley single-diode equation to abstract the entire photovoltaic device as a single diode. The Shockley equation considers a steady state condition and doesn't account for the diode's transient response, which includes the influence of its internal junction, diffusion capacitance and reverse recovery time. In terms of electrical parameters, we assume that the carrier mobility is sufficiently high. The mathematical expression for Shockley diode equation is as follows:

$$J(V) = J_{SC} - j_0\left(e^{\frac{V + JR_s}{nk_BT}} - 1\right) - \frac{V + JR_s}{R_{sh}}$$

where j_0 is the dark saturation current density, n is the ideality factor, k_B is the Boltzmann constant, T is the device temperature, R_s is the series resistance and R_{sh} is the shunt resistance. The R_s and R_{sh} in this work is obtained via inverse parameter tuning from fitting the simulated J-V curves with the experimental results in literature[5]. It should be noted that this equation works for 2T tandem devices and individual sub-cells in 4T devices.

When the J comes to 0, V_{OC} can be obtained via the variant equation:

$$V_{OC} = \frac{nk_BT}{q} ln\left(\frac{J_{SC}}{j_0} + 1\right)$$

As J_{SC} is acquired via the optical simulation, this value of V_{OC} is mainly determined by j_0. The minimum value of the diode saturation current (j_0) is given by the following equation[8]:

$$j_0 = \frac{q\ 15\sigma}{k_B\ \pi^4} T^3 \int_u^\infty \frac{x^2}{e^x - 1} dx$$

where σ represents the Stefan-Boltzmann constant, u equals E_G/kT. This allows us to define the j_0 of perovskite or CIGS active layers with various bandgaps, which establish the functional relationship between the bandgaps and the V_{OC} of cells as well. It should be noted that the V_{OC} for CIGS bottom cells should be amended within the following equation[2]:

$$V_{OC,CT} = V_{OC,CS} - nk_BTln\frac{J_{sc,CS}}{J_{sc,CT}}$$

where CT represents the CIGS bottom sub-cell in a tandem cell, CS represents the CIGS single junction cell. The latter part of this equation represents the V_{OC} discrepancy caused by the perovskite top sub-cell filtering and extra gain from albedo irradiation.

The optical simulation we obtained mainly focuses on calculating the J_{sc} of the sub-cells. However, V_{oc} and FF are also necessary in order to calculate the potential PGD. The state of art perovskite/CIGS tandem solar cells are highly similar in the device configuration. In that case, we can estimate the potential electrical parameters from the state-of-art record within the published studies. In the past few years, ones have summarized the simplified numerical relationship between bandgap and open-circuit voltage reported in the literature, which is used to predict the open-circuit voltage values for different bandgaps[9, 10]. However, we found that while such a simplified proportional relationship seems reasonable within a certain bandgap range (1.5-1.7 eV), perovskites with bandgaps greater than 1.7 eV will undergo irreversible phase separation under illumination. The barrier increases with the expansion of energy level mismatch caused by phase separation, leading to increased open-circuit voltage losses[11]. As a result, the open-circuit voltage of wide-bandgap perovskite solar cells under actual working

conditions is much lower than the value predicted by the simplified proportional relationship.

Due to the open-circuit voltage losses caused by non-radiative recombination and phase separation, which are significant for current perovskite solar cells, it is essential to reflect these in the calculations of optoelectronic performance in this work. We found that *The Perovskite Database* project led by Jacobsson et al. provides valuable data resources for high-throughput analysis[12, 13]. Therefore, after consulting the statistical results of open-circuit voltage losses in *The Perovskite Database* (last updated at the end of 2023), the author has made the following corrections for the V_{OC} losses caused by non-radiative recombination as illustrated in Figure S9. Similarly, Figure S10 depicts the relationship between the open-circuit voltage and bandgap for CIGS cells provided by the latest statistical results[14]. The relationship between the set V_{OC} and bandgap derived from *The perovskite database* is shown in Table S2.

After the relationship between V_{OC} and the bandgaps is given, we can apply the following implicit equations to identify the MPP (maximum power point).

$$V_{mpp} = V_{oc} - \frac{nk_BT}{q} ln\left(\frac{qV_{mpp}}{nk_BT} + 1\right)$$

$$J_{mpp} = J_{sc} - j_0\left(e^{\frac{V_{mpp} + J_{mpp}R_s}{nk_BT}} - 1\right) - \frac{V_{mpp} + J_{mpp}R_s}{R_{sh}}$$

Where V_{mpp} is voltage at MPP, and J_{mpp} is the current density at MPP. After the MPP is confirmed, we can calculate the fill factor (FF) with:

$$FF = \frac{V_{mpp} \times J_{mpp}}{V_{oc} \times J_{SC}}$$

By combining with the electrical stimulation of the experimental 2T-Monofacial J-V curve (Figure S11

& S12) and the optimized result, we can identify the R_s and R_{sh} for the perovskite/CIGS tandem solar cells, and the resulting FF distribution for 2T configuration (Figure. S13) and for sub-cells in 4T configuration (Figure. S14) is acquired.

3. Energy Yield modelling

Without considering the efficiency degradation of photovoltaic devices within a year, the prediction of annual energy yield (EY) of photovoltaic devices takes into account the deployment location's latitude, longitude and weather conditions. The calculation of irradiance relies on typical meteorological year (TMY3) data with hourly resolved spectrally information. A simple model, utilizing the simple model of the atmospheric radiative transfer of sunshine (SMARTS), is employed to determine clear-sky irradiance, considering both specular reflection and diffuse fraction, which enables the establishment of a local solar irradiance model based on the solar zenith and azimuth angles throughout each hour, as well as the local meteorological conditions. The TMY3 dataset is accessible at the SRRL SSIMG Web site[15]. In this study, we use TMY3 data in the Miami area as an example, showcasing the spectral variations throughout a day, as illustrated in Figure S24 and Figure S25. Once we obtain the spectral irradiance data for all 8760 hours in a year, we can simulate the J-V curves to calculate the maximum power point of the device for each hour. By summing the power output from each hour, we can determine the EY by the photovoltaic device over the course of a year.

To provide an intuitive showcase of the EY potential worldwide, we partitioned the world into 6.48×10^8 blocks using the Solargis algorithm (43200×15000 grids at 1 km intervals). These grids were then correlated with the output power derived from high-throughput calculations, aligning with both

solar irradiance conditions (as shown in Figure S29) across various global regions and the temperature distribution (depicted in Figure S30). The temperature coefficient for PVSK and CIGS sub-cells are set to be -0.22% K^{-1} and -0.38% K^{-1} respectively, according to Jošt et al[2]. The GIS data originate from Global Solar Atlas[16] *© 2020 The World Bank, Source: Global Solar Atlas 2.0, Solar resource data: Solargis*.

4. High throughput calculation method

During the global optimization process, many functional layers in the cell stack do not require high-throughput optoelectronic simulation to determine their optimal thickness. For example, in the perovskite sub-cell, the thicknesses of the carrier transport layer materials such as NiOx and C60, the buffer layer SnO2, and the transparent conductive electrode IZO, only contribute to increased parasitic optical absorption, leading to photocurrent loss. Therefore, for these functional layers, their material types and thicknesses can be fixed at the minimum thickness reported in the literature that meets their functional requirements, without further iteration.

In terms of the boundary conditions, the bandgap for perovskite is determined to range from 1.20 eV to 2.01 eV while the bandgap for CIGS ranges from1.01 eV to 1.20 eV. Although the band gap of CIGS can be tuned from 1.01-1.67 eV[17], the best band gap for bottom sub-cell in a bifacial system should be around 1.12 eV according to De Wolf et al[18].

With the assistance of a supercomputing platform, we systematically explored all combinations of perovskite and CIGS sub-cell bandgaps within the specified range, using a step size of 0.03 eV and 0.01 eV, respectively. The thickness of the perovskite layer was varied in 10 nm increments. We successfully ported the EY calc software to the Linux system and developed scripts specifically designed to initiate high-throughput calculations. Leveraging the computational power of the supercomputing center's servers, we concurrently utilizing 10 nodes with a total of 640 cores (AMD EPYC 7452) for parallel computing, enabled us to complete calculations for several hundred thousand combinations within 1 to 2 hours.

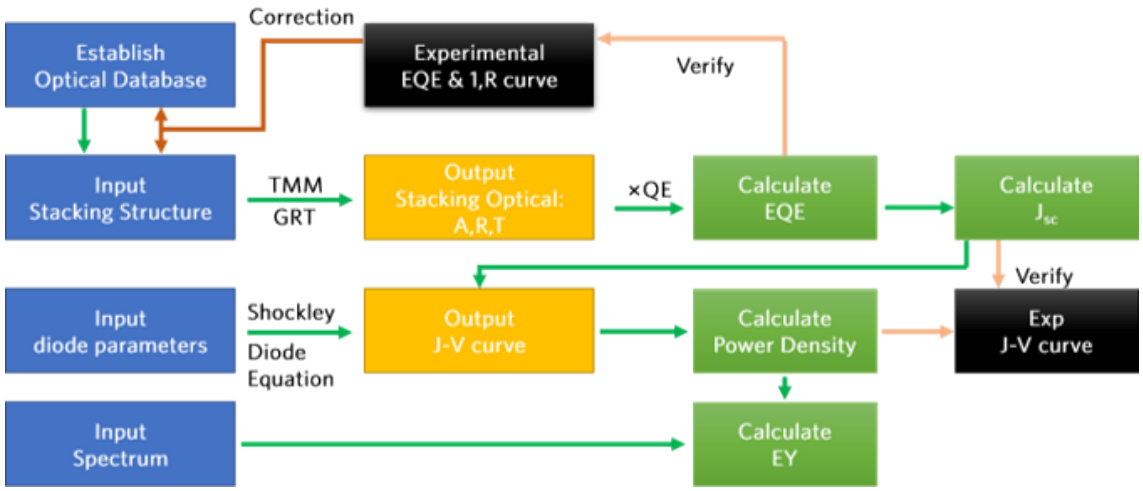

Figure S1. Methodology of transfer matrix method optical simulation and potential power generation calculation.

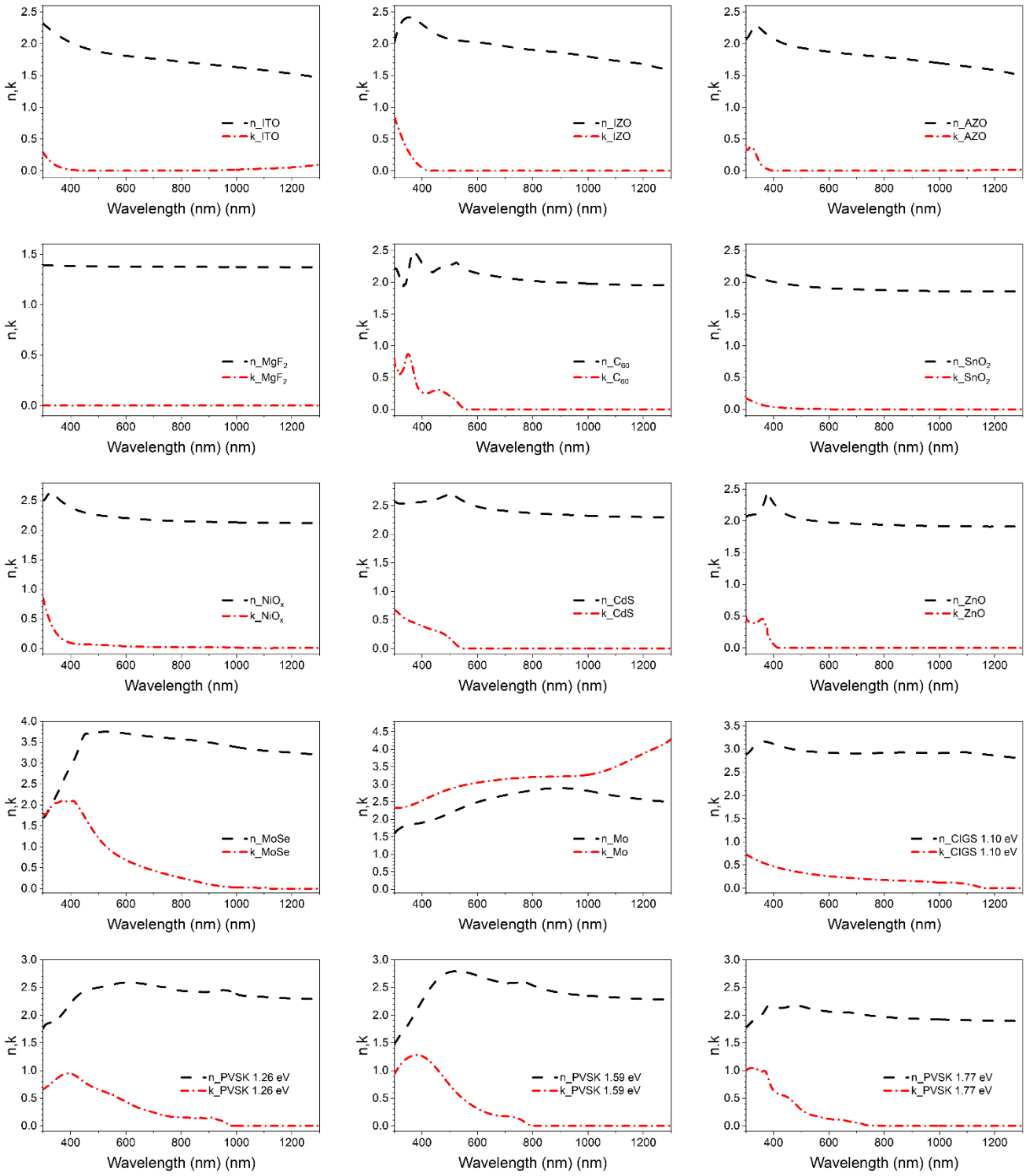

Figure S2. The complex refractive indices of all materials used in this study. The data sources can be found in Table S1.

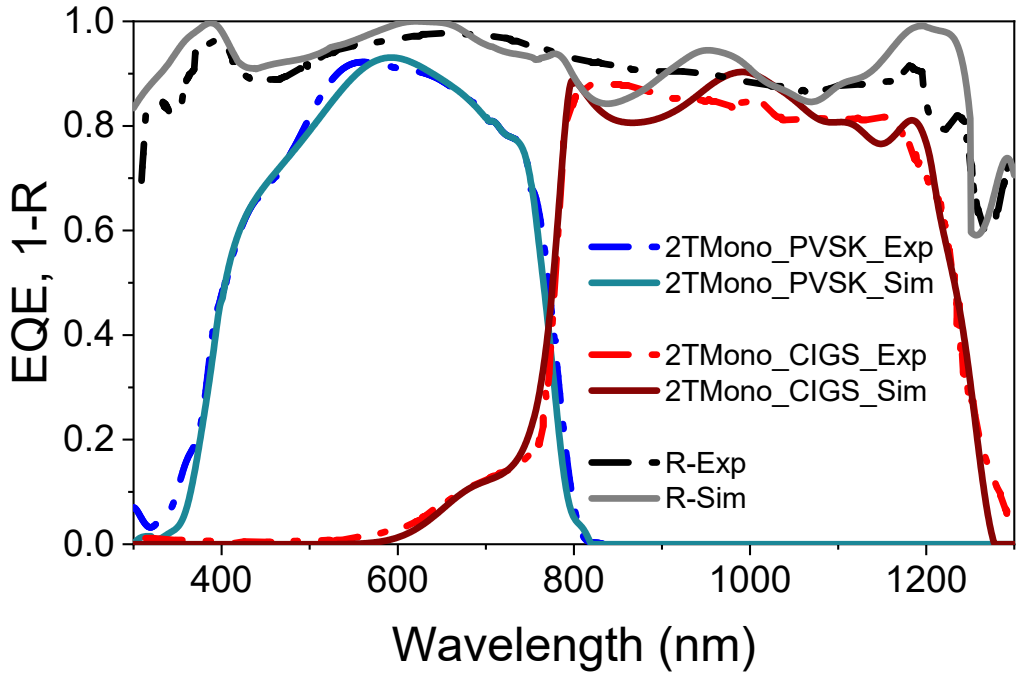

Figure S3. Comparison of the simulated reflectance and EQE with the experimental results for PVSK/CIGS tandem solar cells;

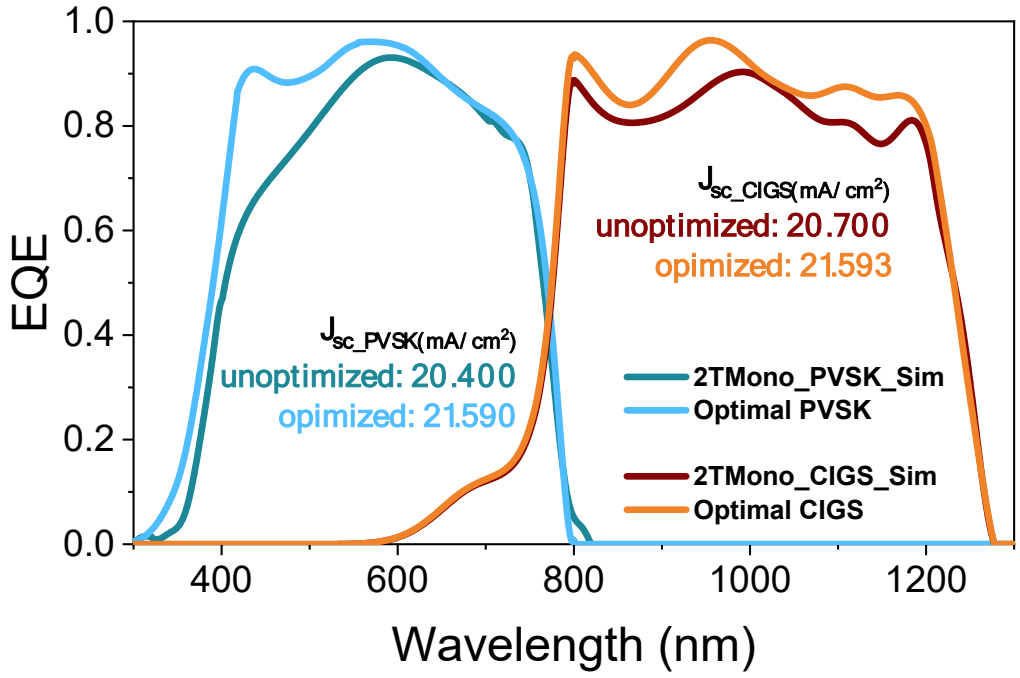

Figure S4. Optimized monofacial PVSK/CIGS tandem cell configuration compared with the original simulation results.

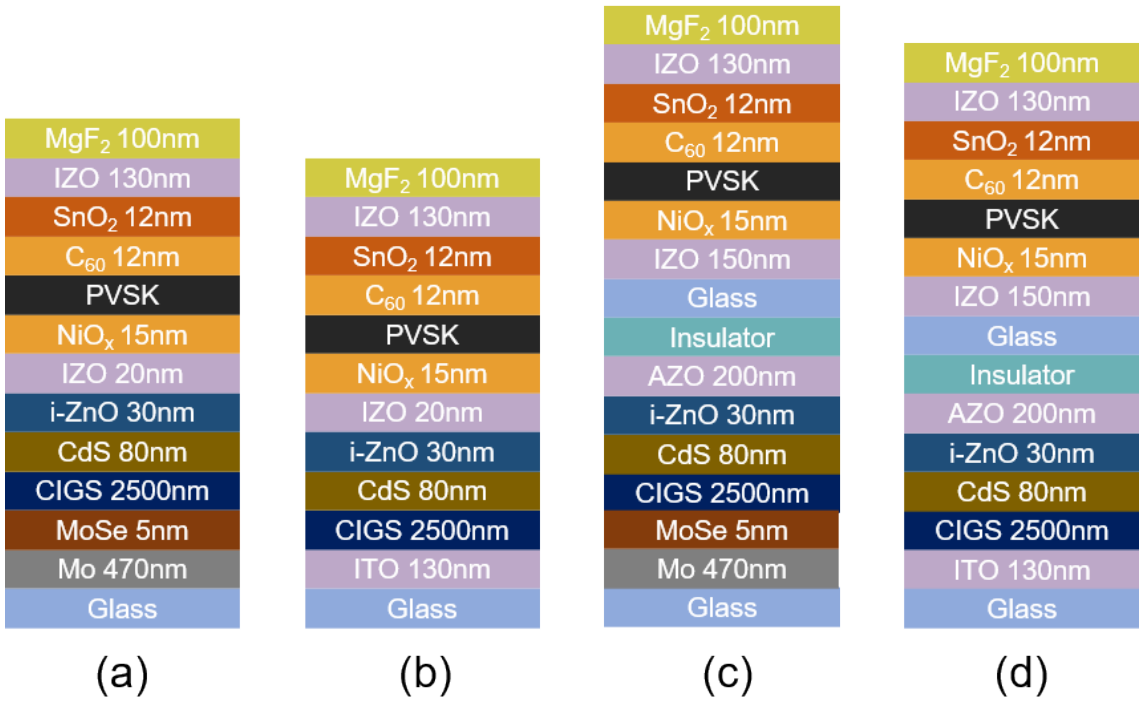

Figure S5. Optimal stack configurations for (a) 2T monofacial, (b)2T bifacial, (c) 4T Monofacial and (d) 4T bifacial perovskite/CIGS tandem solar cells.

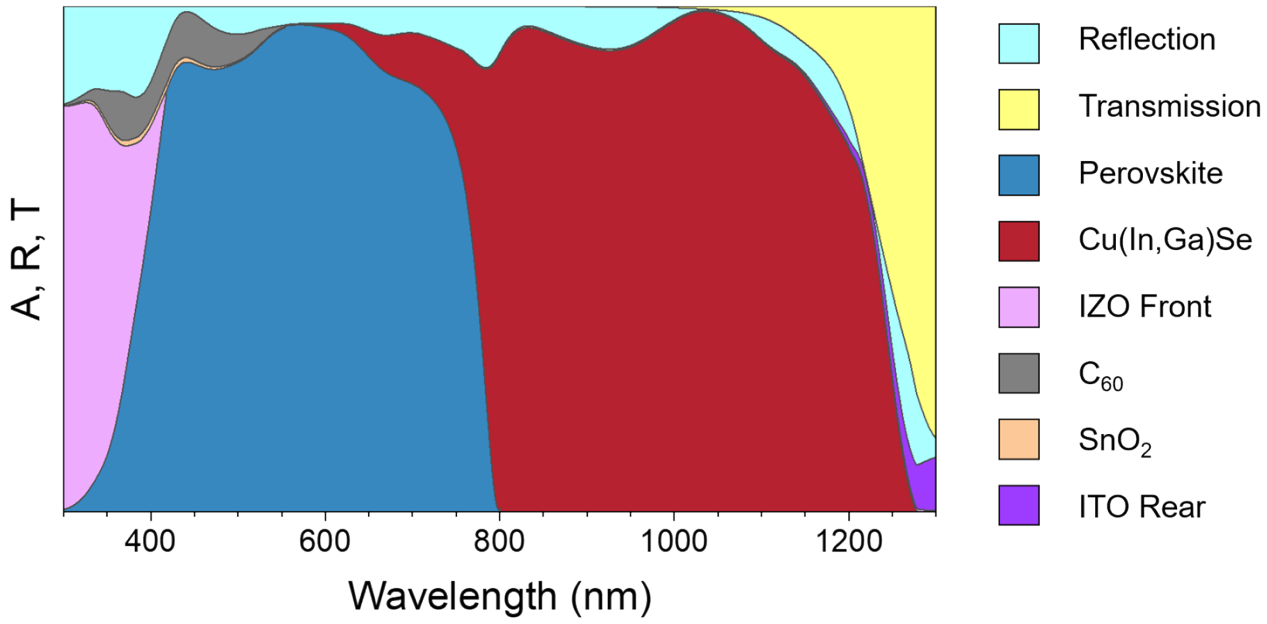

Figure S6. Absorptance spectra and parasitic losses for bifacial cell with front side illumination.

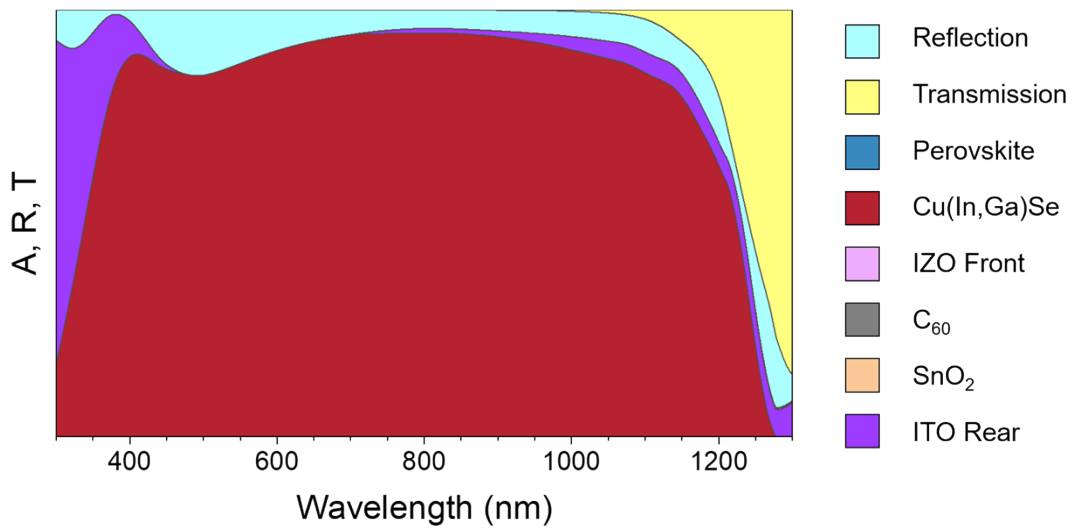

Figure S7. Absorptance spectra and parasitic losses for bifacial cell with rear side illumination.

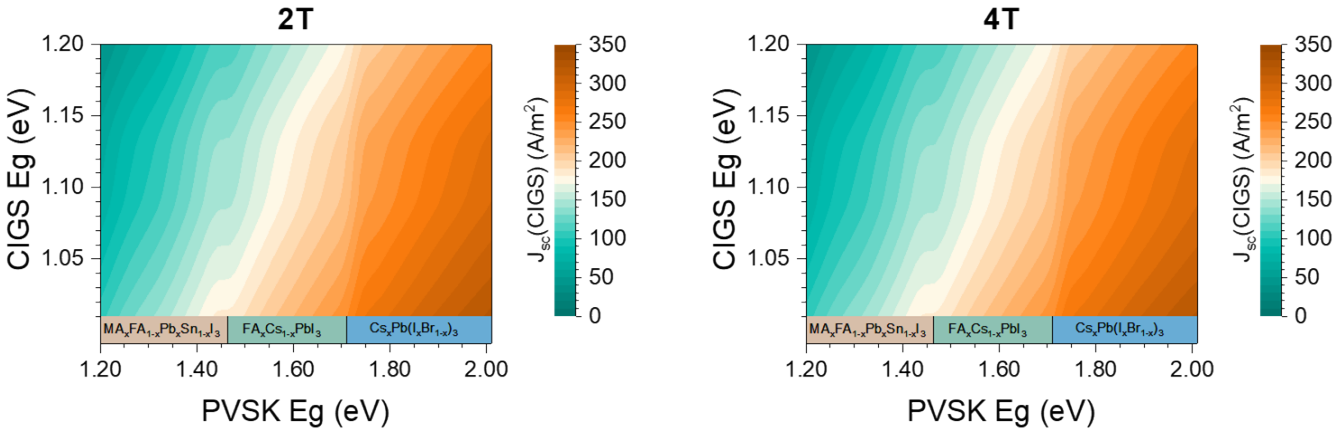

Figure S8. The J_{sc} comparison of PVSK filtered CIGS sub-cells between 2T and 4T configuration in the bifacial PVSK/CIGS tandem. The thickness for perovskite is held constant at 600 nm and the device configuration are consistent with Figure S4 (b) and (d).

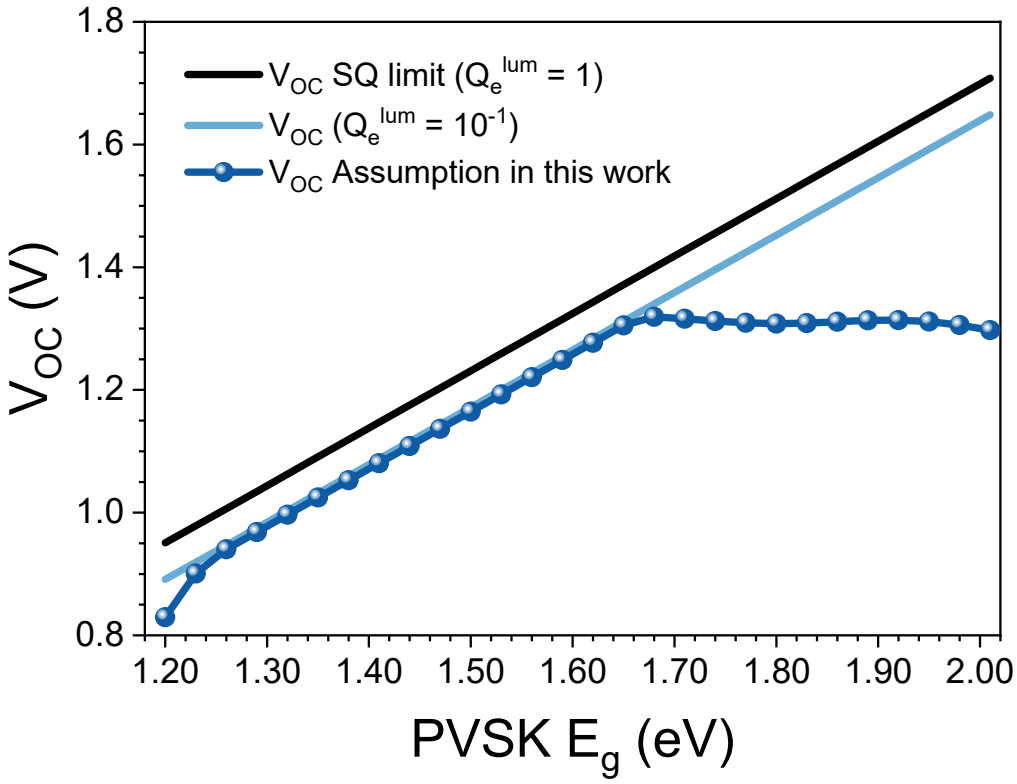

Figure S9. Projected relationship of the perovskite bandgaps and open-circuit voltage.

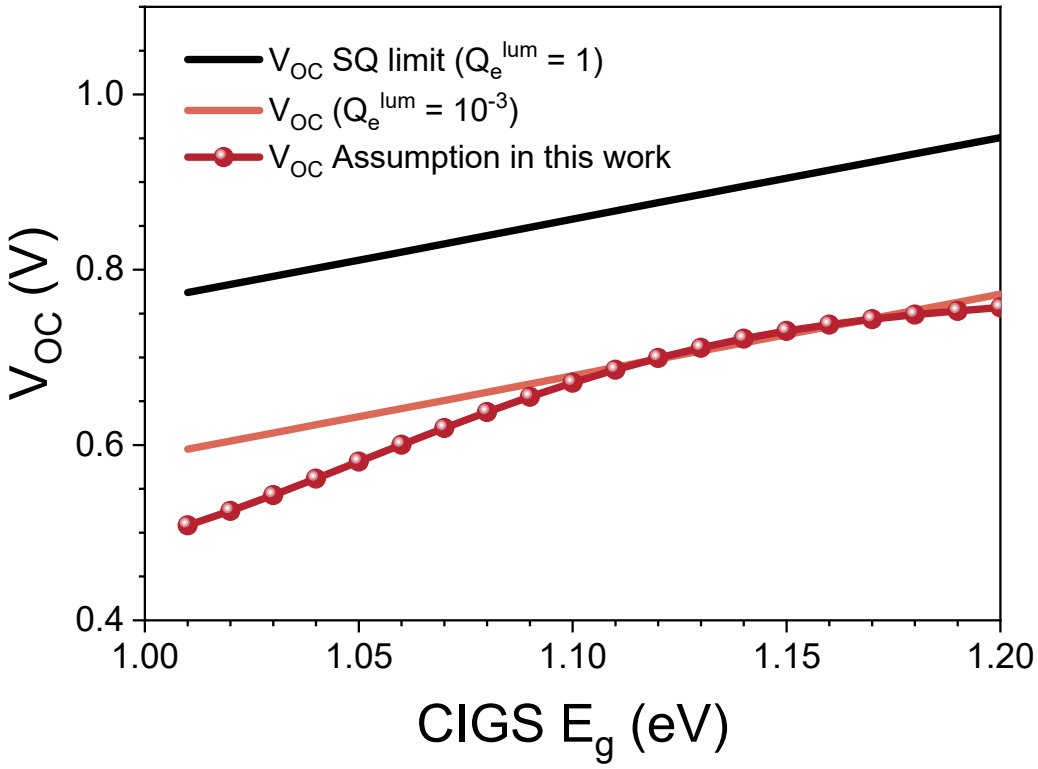

Figure S10. Projected relationship of the CIGS bandgaps and open-circuit voltage.

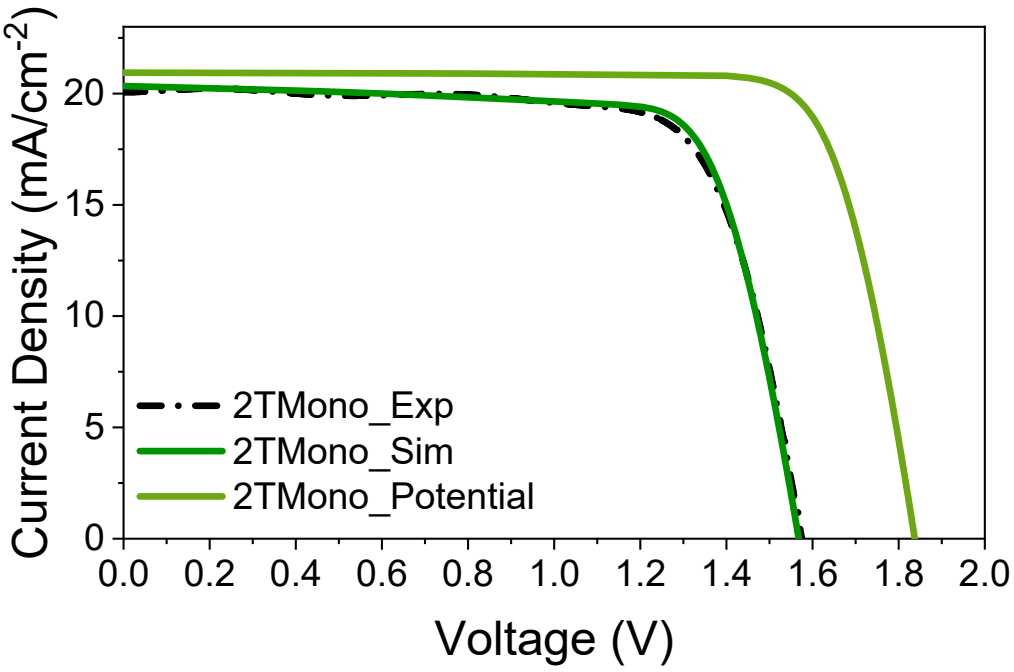

Figure S11. The experiment result and optimal simulation of 2T PVSK/CIGS tandem solar cells.

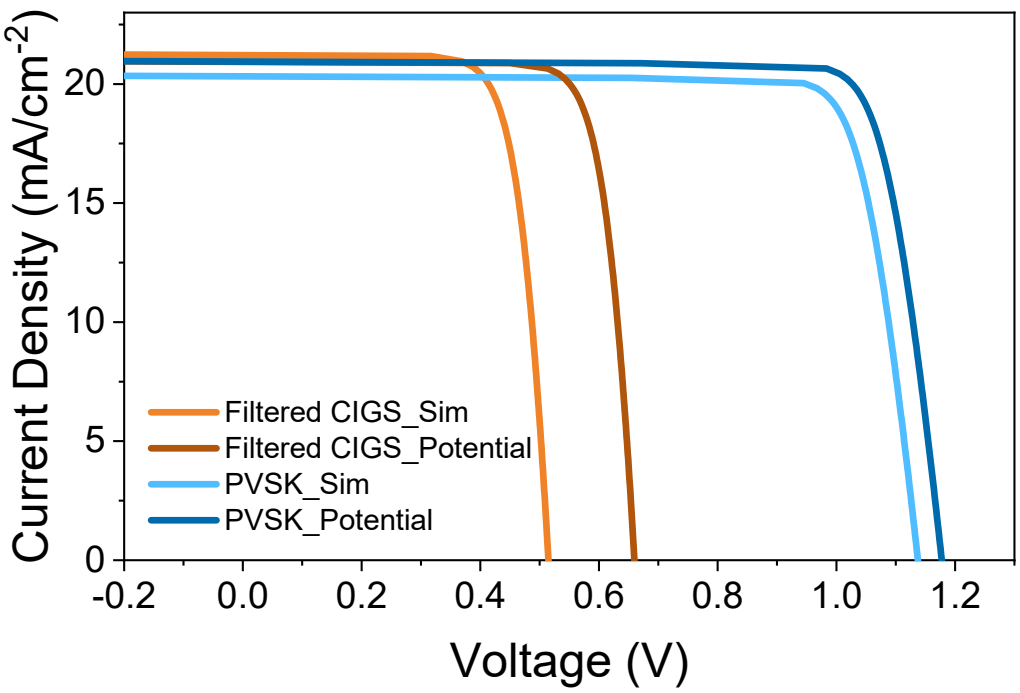

Figure S12. The experimental and optimal potentials J-V simulation for each sub-cell for PVSK/CIGS tandems. The electrical parameters were determined based on the study conducted by Paetzold et al[5]. The single-junction CIS cell had a bandgap of approximately 1.01 eV, with an open-circuit voltage of 0.53 V. The PVSK/CIGS tandem cell demonstrated an impressive PCE of 24.9% (certified at 23.5%), representing one of the highest experimental results achieved to date.

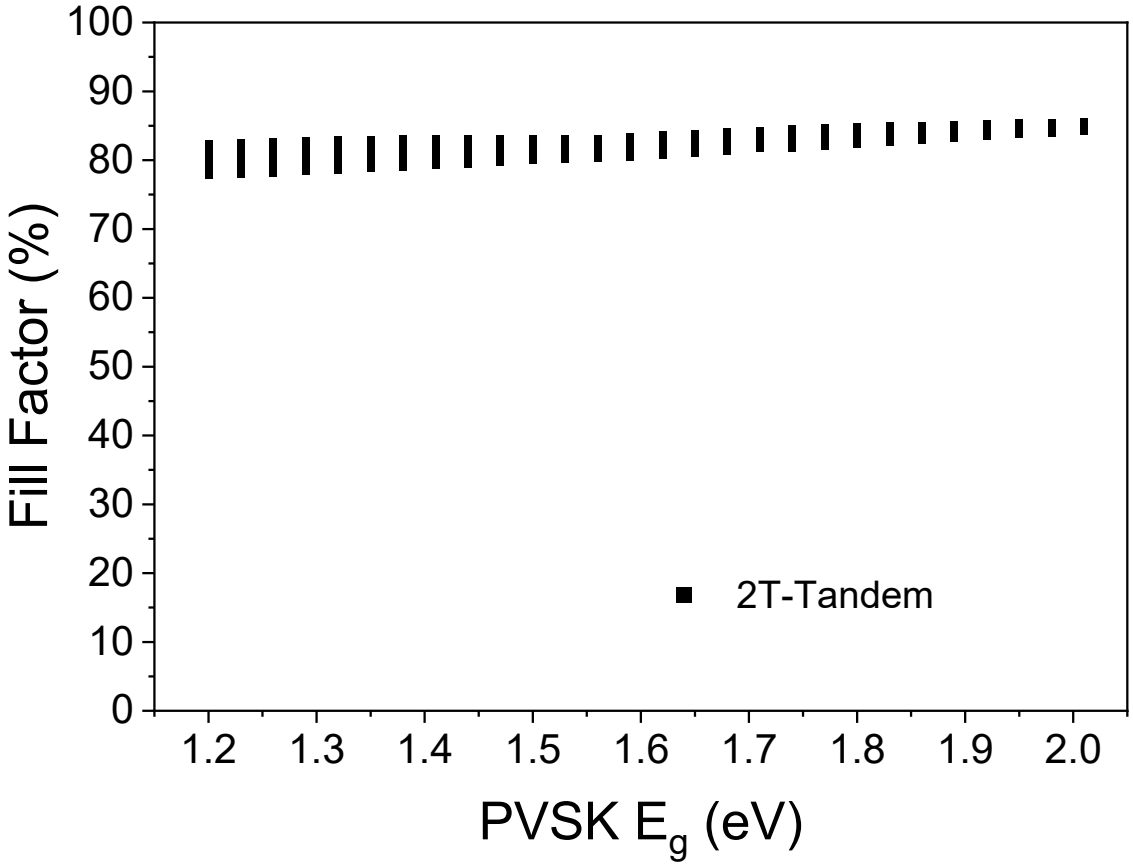

Figure S13. Fill factor distribution for 2T PVSK/CIGS tandem solar cells.

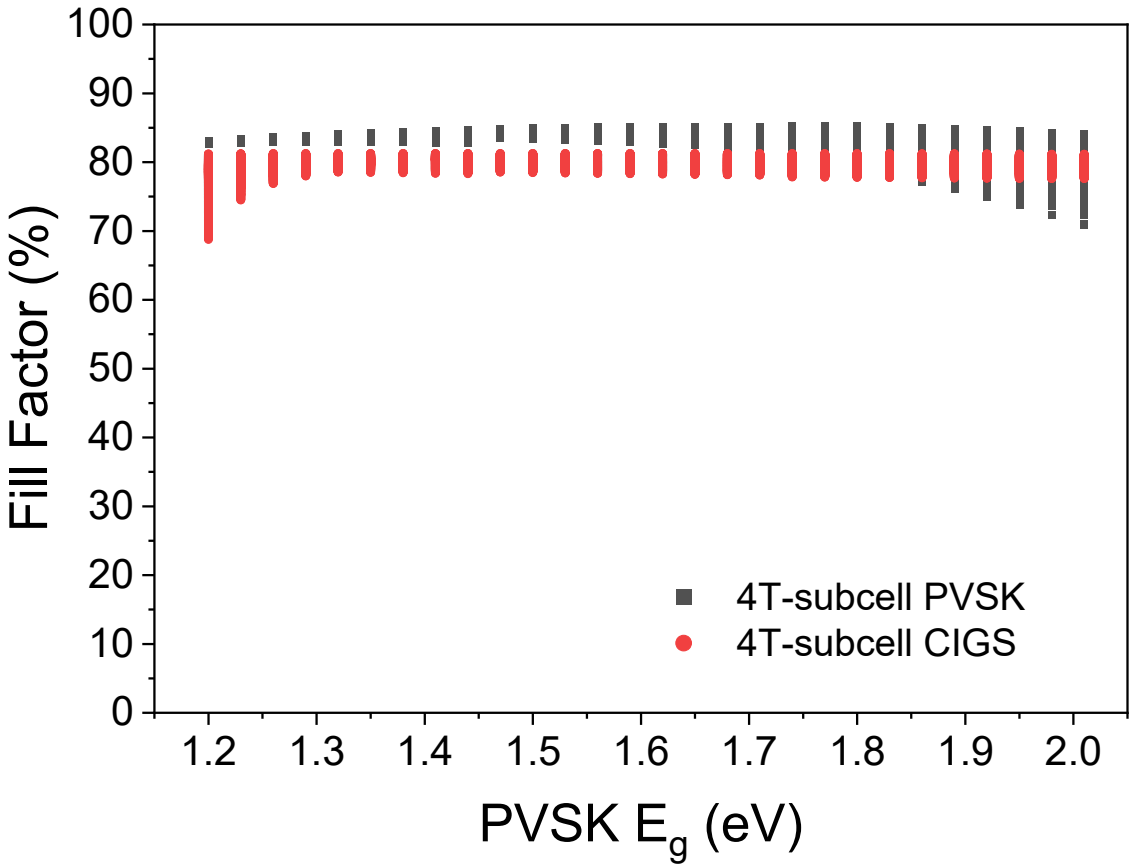

Figure S14. Fill factor distribution for the perovskite and CIGS sub-cells for 4T PVSK/CIGS tandem solar cells.

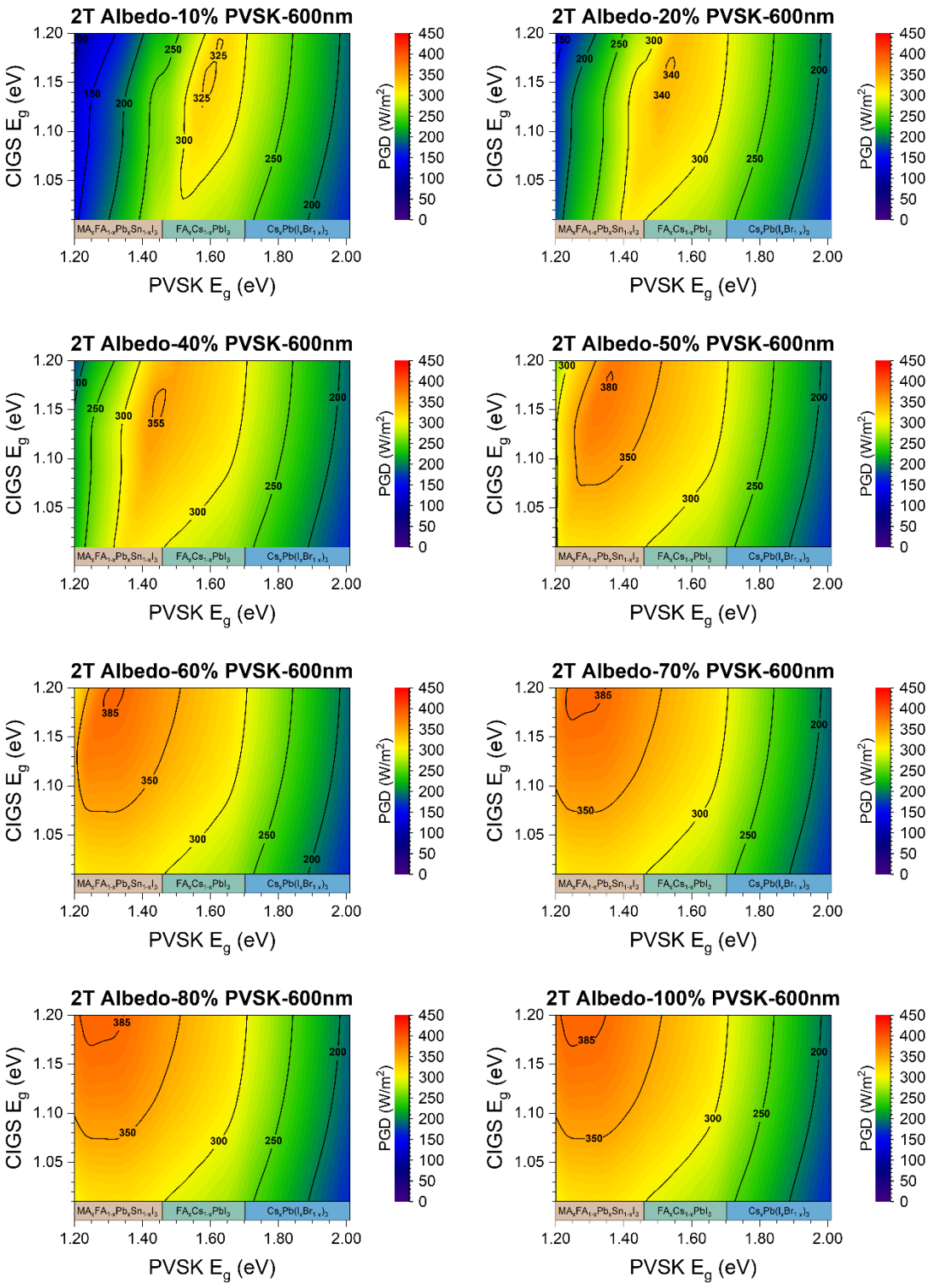

Figure S15. Power generation density as a function of the bandgaps of perovskite and CIGS under various albedo illumination.

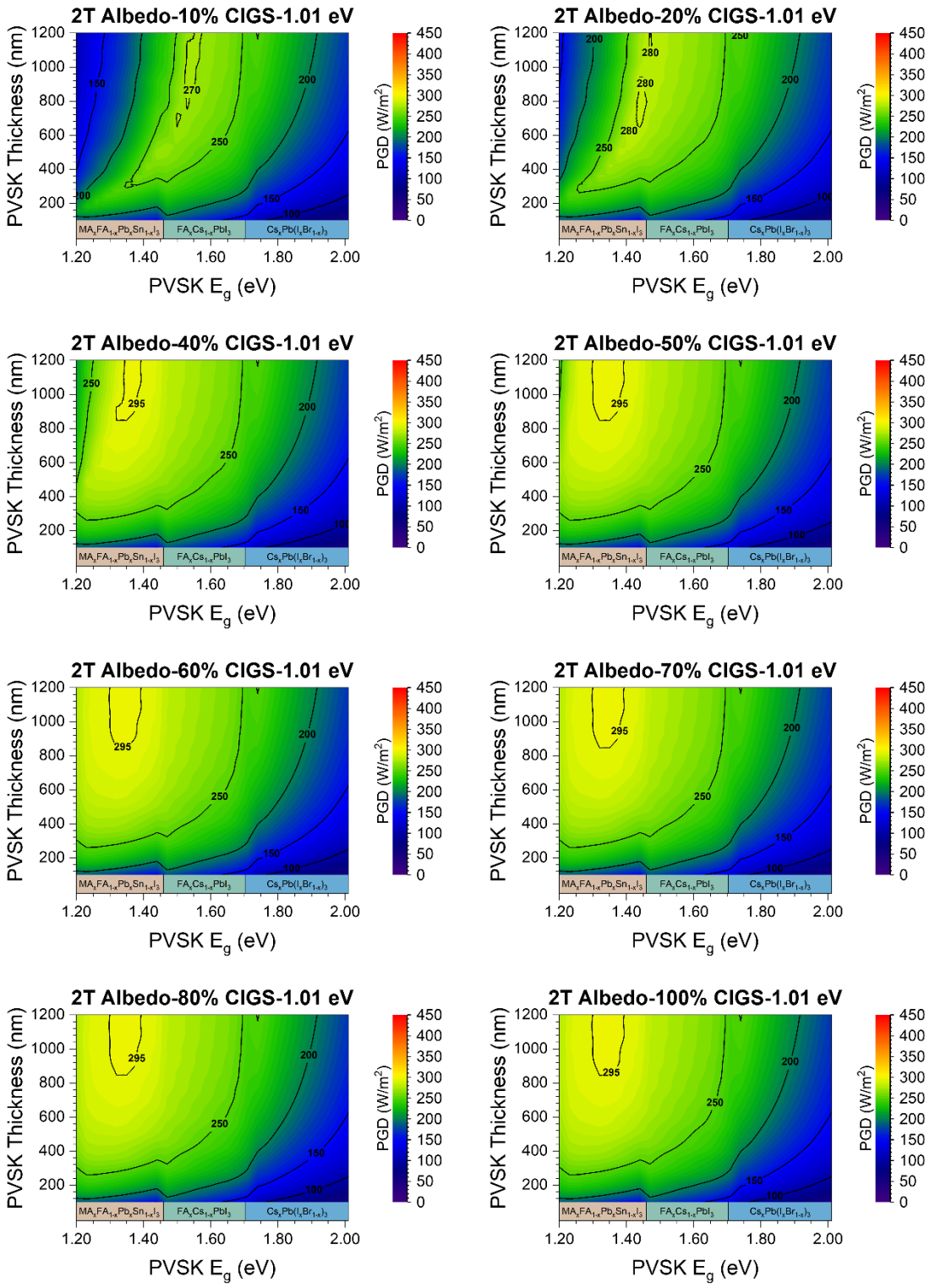

Figure S16. Power generation density as a function of the bandgaps and thickness of perovskite under various albedo illumination.

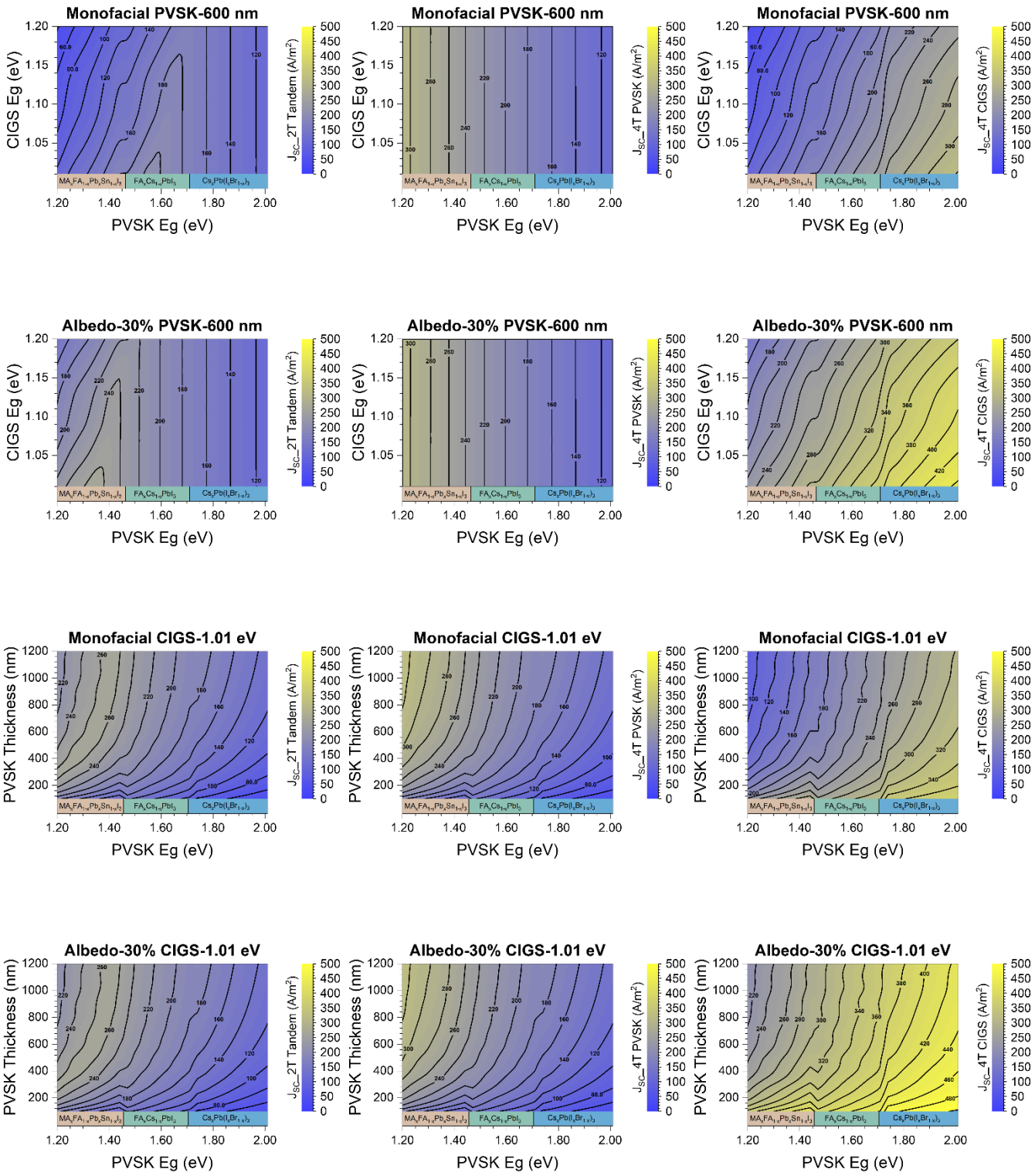

Figure S17. The distribution of J_{SC} as a function of bandgap and thickness under the conditions corresponding to Figure 2 in the main text.

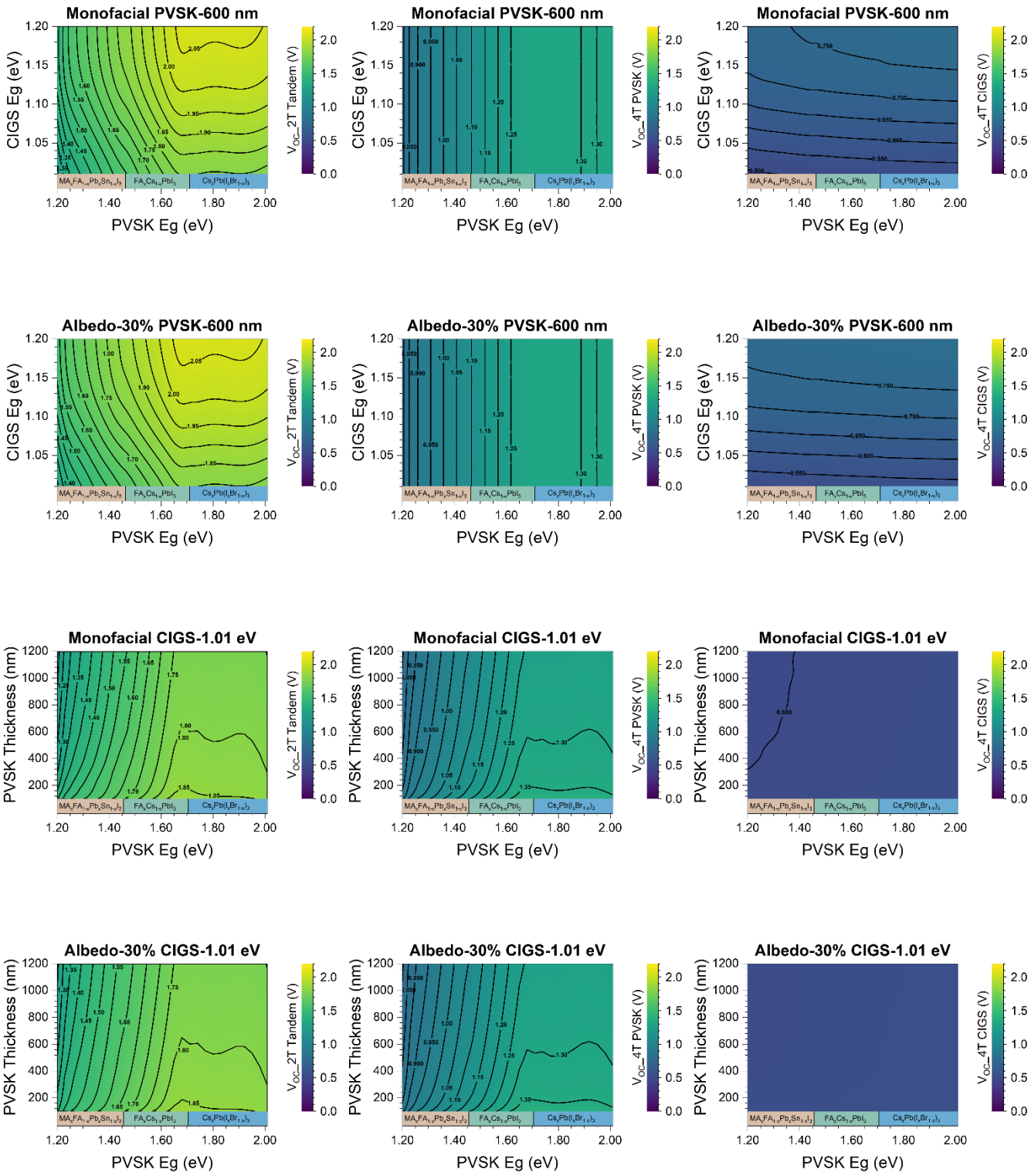

Figure S18. The distribution of V_{OC} as a function of bandgap and thickness under the conditions corresponding to Figure 2 in the main text.

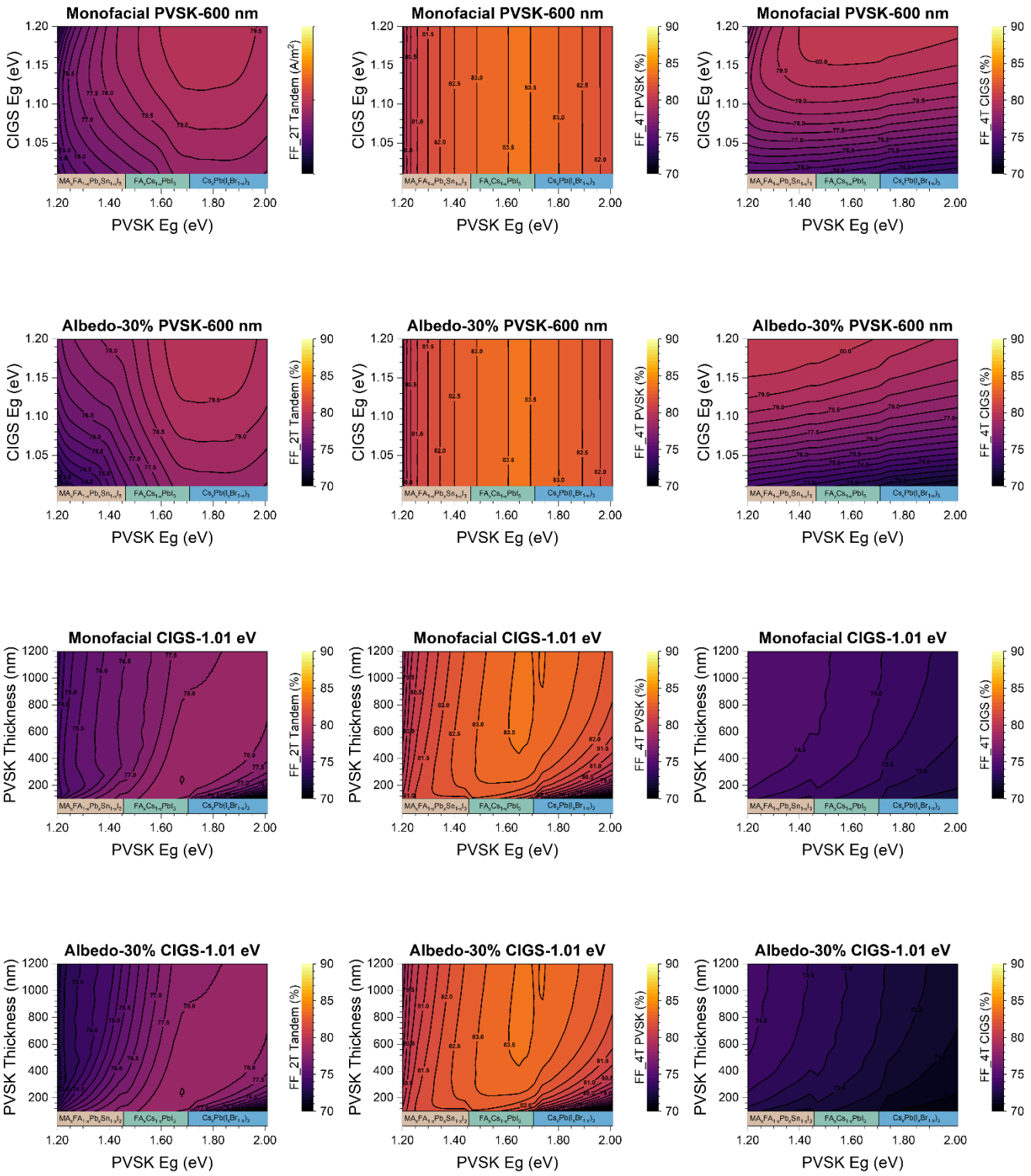

Figure S19. The distribution of FF as a function of bandgap and thickness under the conditions corresponding to Figure 2 in the main text.

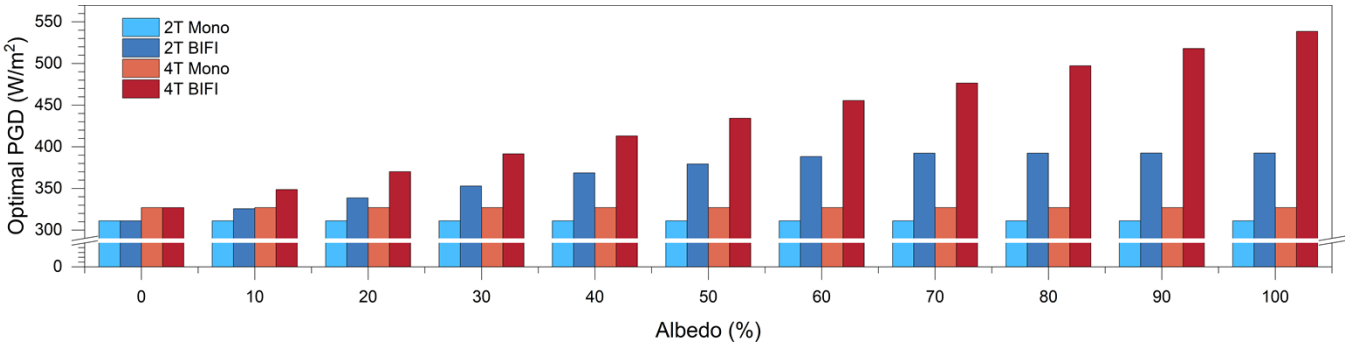

Figure S20. The potential PGD for various device configurations under different albedo illumination.

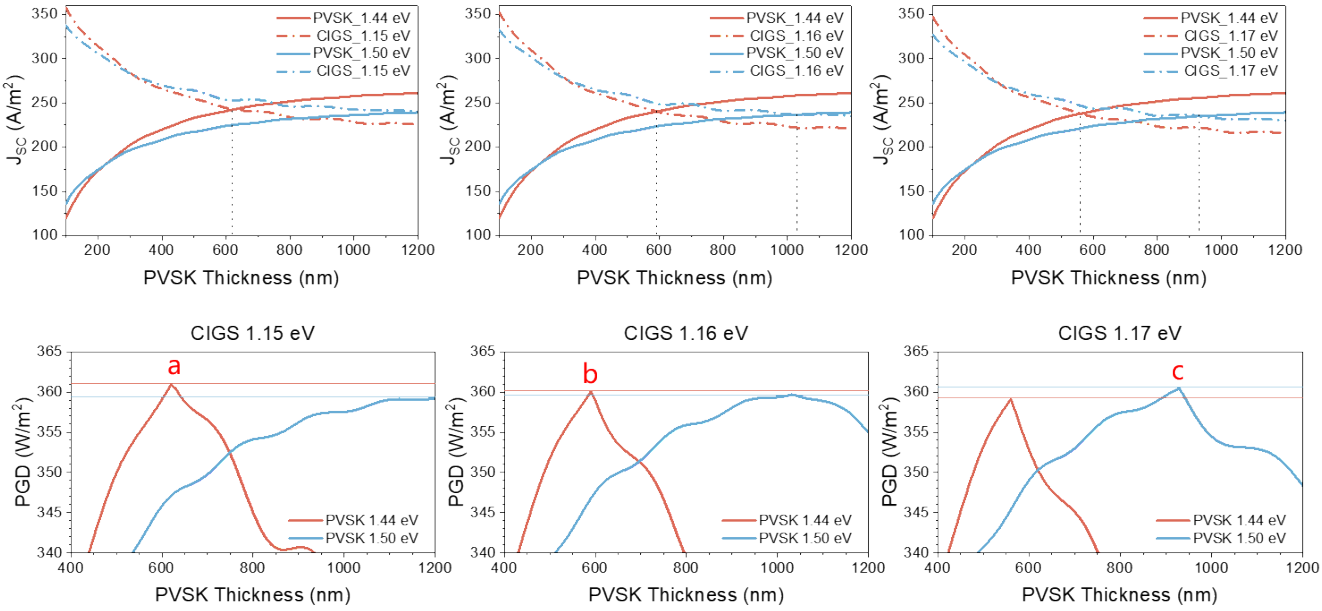

Figure S21. The relationship between current matching and PGD for perovskite materials with bandgaps of 1.44 eV and 1.50 eV when varying the thickness on different bandgaps CIGS substrates.

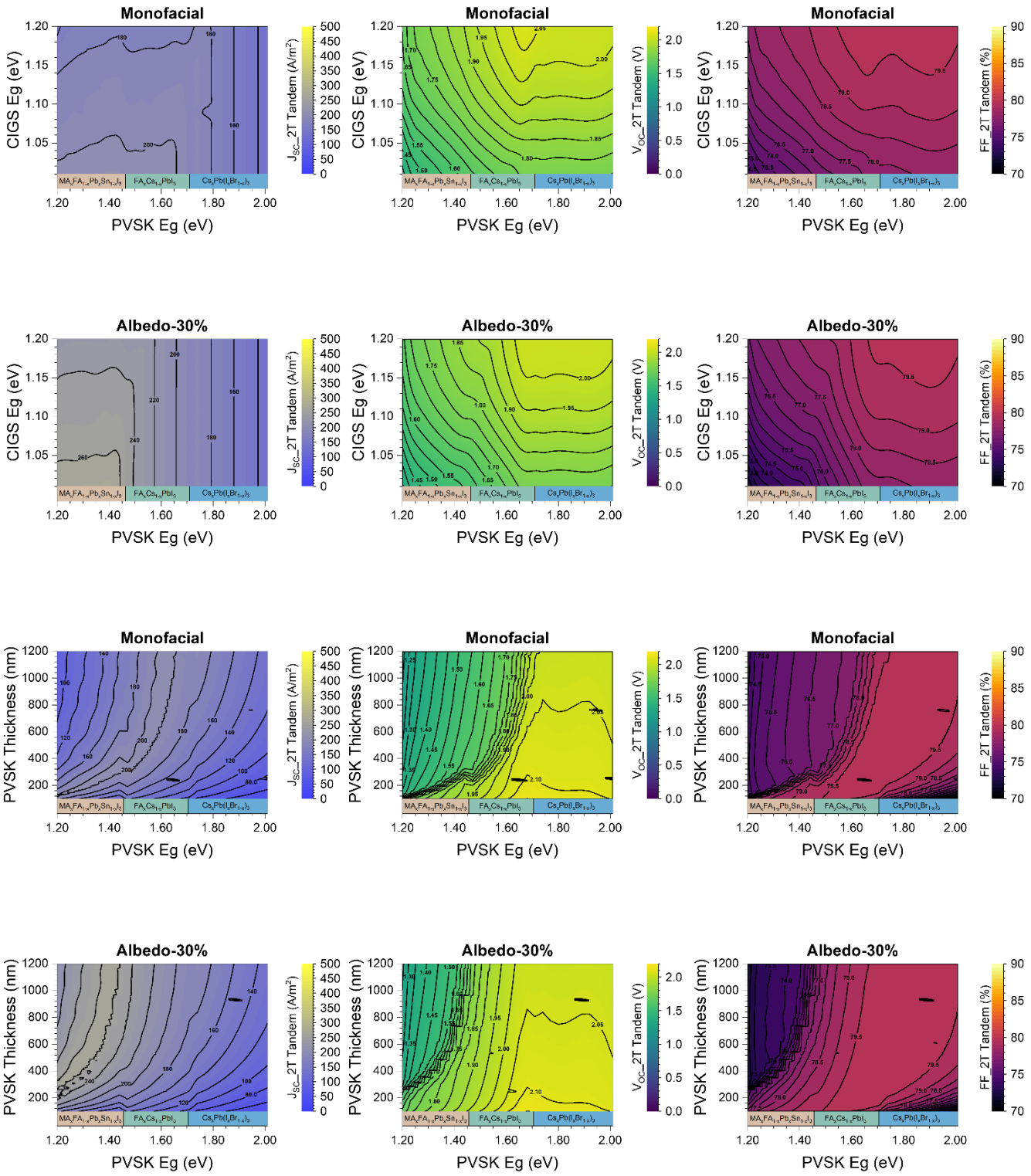

Figure S22. The distribution of J_{SC}, V_{OC} and FF as a function of bandgap and thickness under the conditions corresponding to Figure 4 in the main text.

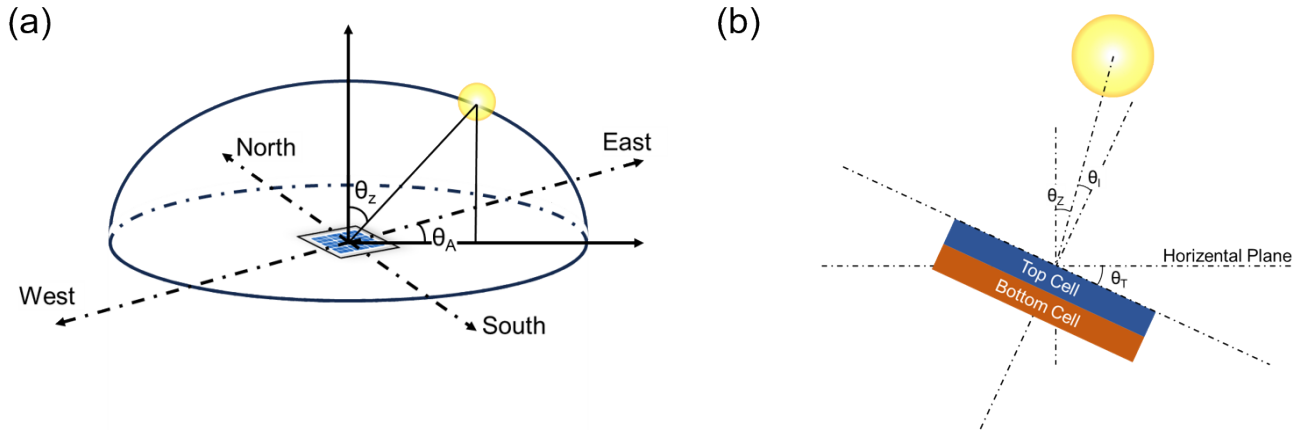

Figure S23. Diagram depicting the relationship between the orientation of the light source and the incident angle, where θ_Z, θ_A, θ_I, θ_T represent the zenith angle, azimuth angle, incident angle and tilt angle respectively. θ_Z, θ_A determines the exact directions of the sun and vary with location and time. θ_T represent the angle between horizontal plane and the surface of solar cell panel. The light incident angle θ_I is actually calculated by the three angles mentioned above.

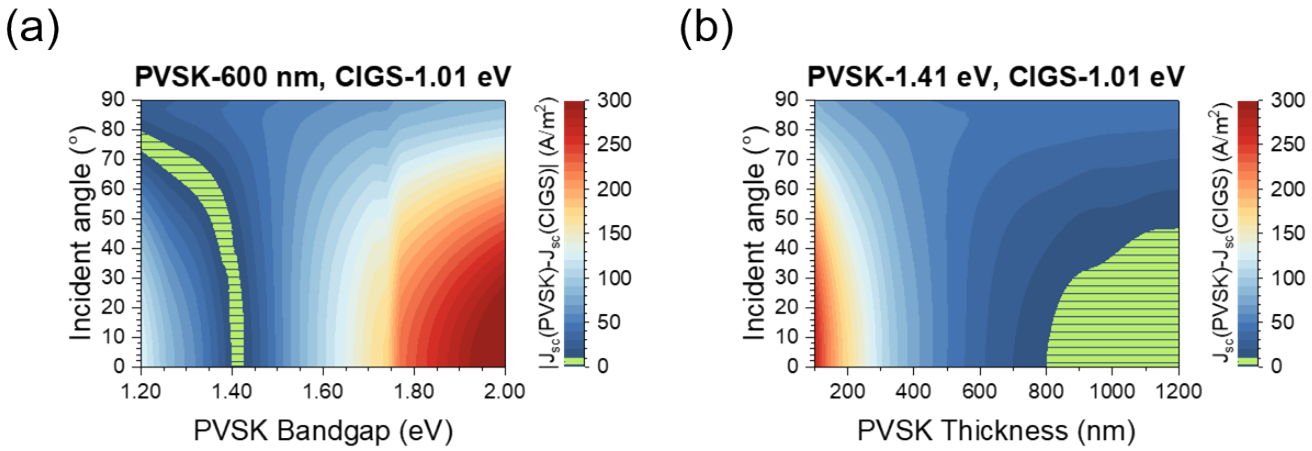

Figure S24. The short-circuit current density mismatching index as a function of incident angle. The albedo light intensity is set to be 30%, the CIGS bottom sub-cell is fixed at 1.01 eV with (a) the thickness of perovskite fixed at 600 nm and (b) the bandgap of perovskite held constant at 1.41 eV. The green shaded areas represent the difference in current density between the two sub-cells are less than 10 A/m^2.

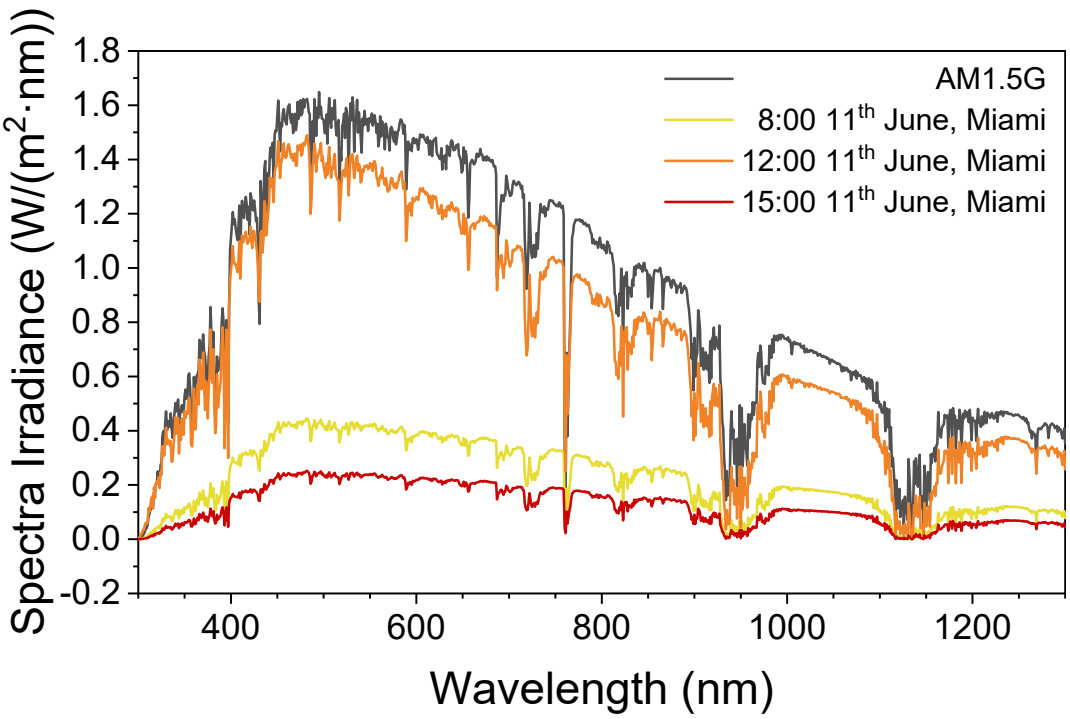

Figure S25. The comparison of direct irradiance spectra between AM1.5G and a day in June in the Miami area.

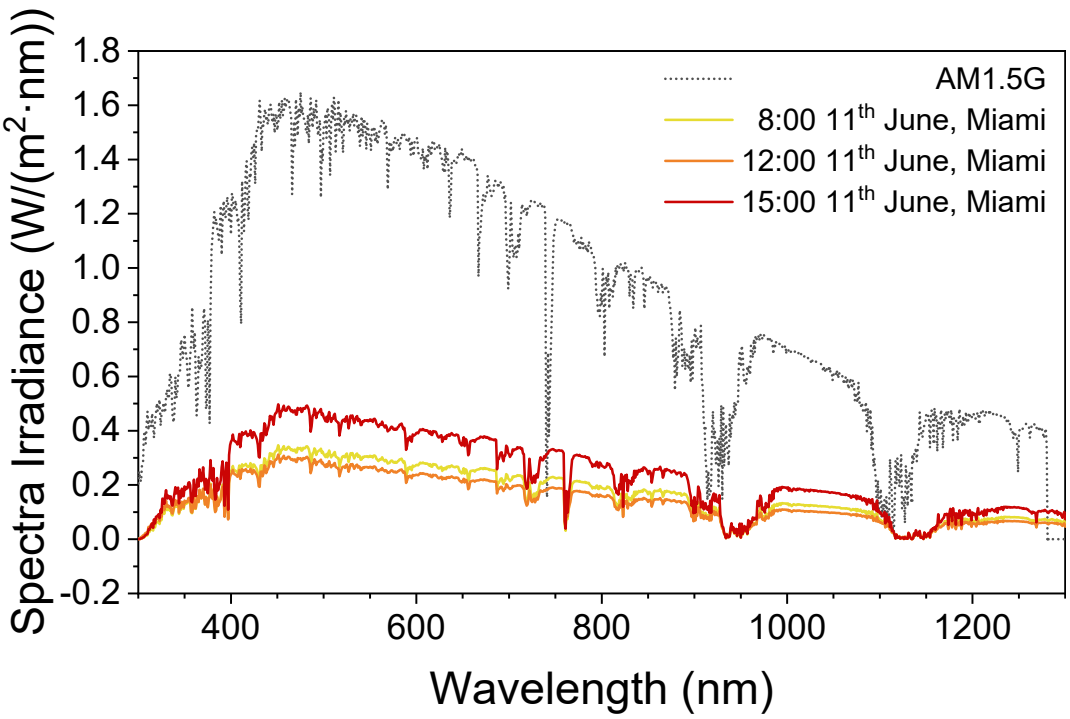

Figure S26. The comparison between AM1.5G and diffusion irradiance spectra in a day of June in the Miami area.

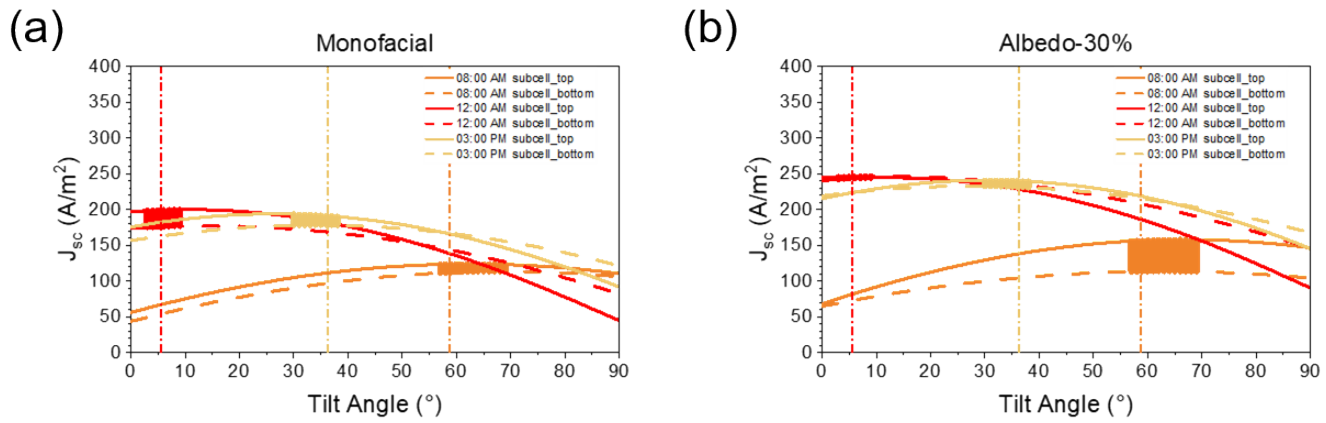

Figure S27. The short-circuit current density as a function of tilt angle.

The configuration for active layer is set to be 1.59 eV, 600 nm for perovskite top sub-cell and 1.01 eV, 2500 nm for CIGS bottom sub-cell (Monofacial), 1.41 eV, 600 nm for perovskite top sub-cell and 1.01 eV, 2500 nm for CIGS bottom sub-cell (Bifacial, 30% albedo). The panel is set to follow the azimuth of the sun (single-axis tracking) with a fixed tilt angle.

The shaded areas in the graph represent the angles at which the lower values of the current density for both sub-cells reach their maximum, indicating the optimal performance range for solar panel inclination at these angles.

The respective positions of the solar zenith angles at that time are indicated by lines of corresponding colors and the real-world irradiance data of that day are summarized in Table S5.

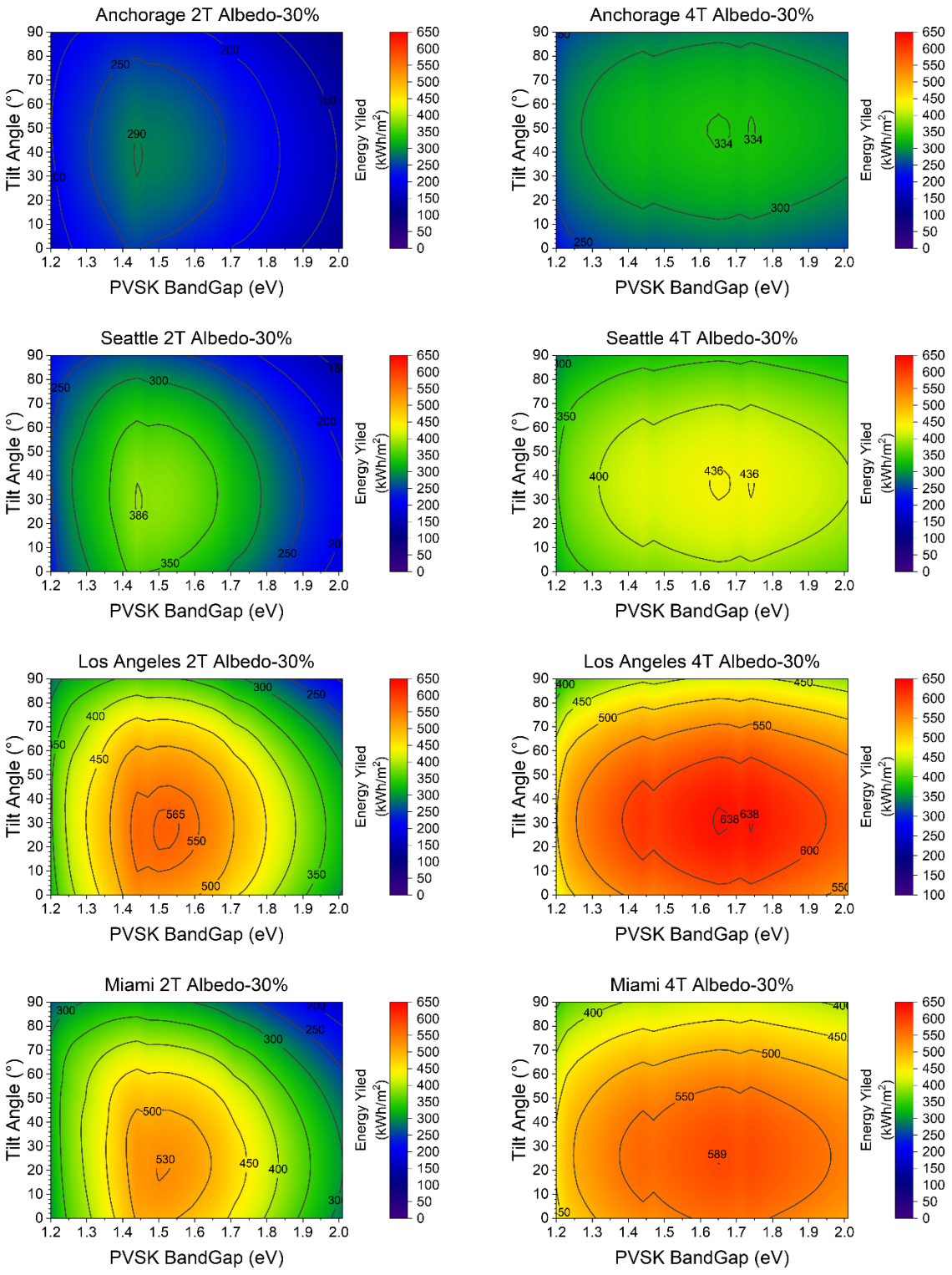

Figure S28. The impact of different perovskite bandgaps and tilt angles on the energy yield analyzed across four cities at different latitudes using the TMY3 dataset.

Clearly, solar panels could output the maximum power generation when positioned at an angle close to the local latitude.

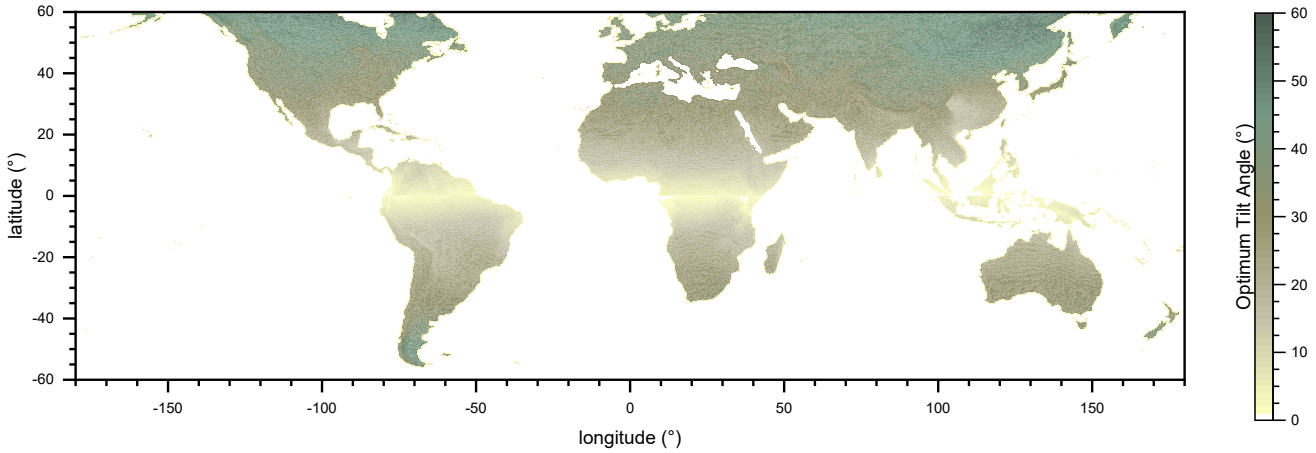

Figure S29. Optimum tilt angle for solar panels across the world.

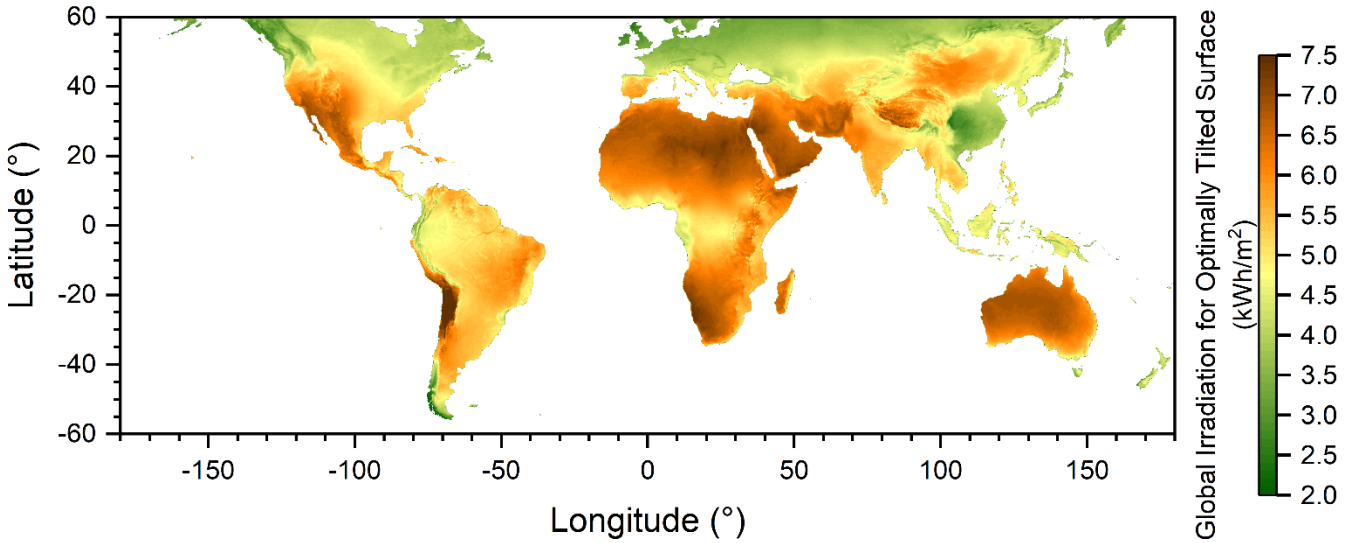

Figure S30. Long-term average of daily totals of global irradiation at an optimum tilt (GTI) in kWh/m^2, covering the period from 1994 to 2022. Positive values in longitude indicate the eastern hemisphere, while positive axis values in latitude signify the northern hemisphere and vice versa.

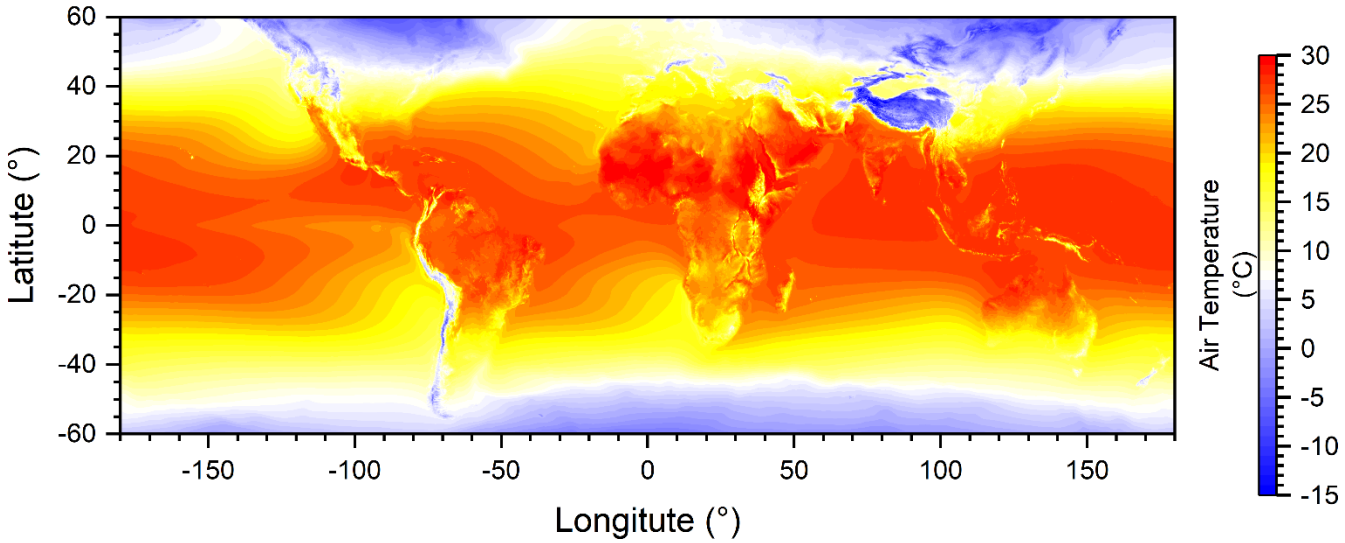

Figure S31. The global distribution of long-term yearly average air temperatures at 2 m above ground level (spanning from 1994 to 2022). Positive values in longitude indicate the eastern hemisphere, while positive axis values in latitude signify the northern hemisphere and vice versa.

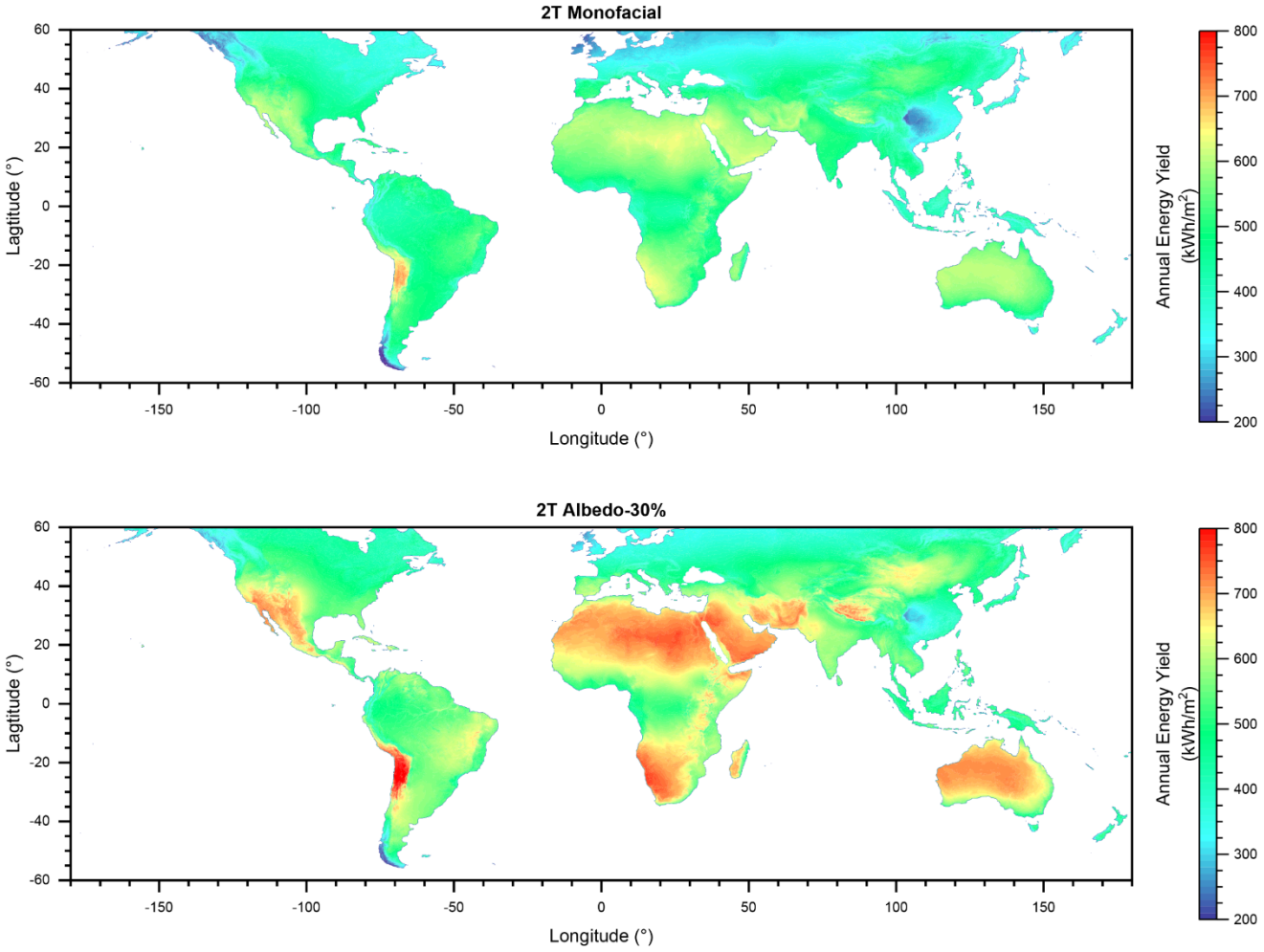

Figure S32. The worldwide EY potential for 2T configuration PVSK/CIGS tandem cell.

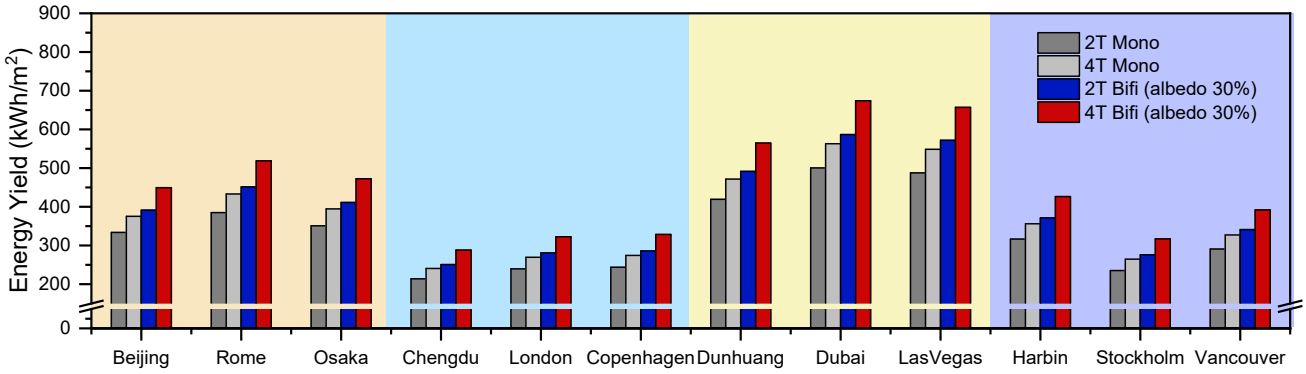

Figure S33. Annual energy yield prediction of perovskite/CIGS tandem solar cells with various climates. For each location, the bandgap combination and thickness of perovskite top sub-cells are optimized to achieve the best performance.

Table S1. Optical parameters sources.

Materials	Literature	n	k
Air	NA	1.000	0.000
Glass	NA	1.500	0.000
POE	[19]	1.515-1.646	0.000
MgF_2	[20]	1.372-1.393	0.000
ITO	[21]	1.472-2.349	0.000-0.305
IZO	[22]	1.604-2.415	0.000-0.845
AZO	[23]	1.500-2.281	0.000-0.380
C_{60}	[2]	1.398-2.470	0.000-0.870
SnO_2	[22]	1.853-2.119	0.000-0.176
NiO_x	[5]	2.118-2.639	0.000-0.851
$CsPbI_3$	[24]	1.858-2.186	0.000-1.101
$FAPbI_3$	[25]	1.047-2.792	0.000-1.281
$FAPb_{0.5}Sn_{0.5}I_3$	[26]	1.743-2.591	0.000-1.267
CdS	[23]	2.300-2.705	0.000-0.679
ZnO	[27]	1.911-2.435	0.000-0.493
CI(G)S	[28]	2.769-3.169	0.000-1.403
$MoSe_2$	[29]	1.692-3.750	0.000-2.106
Mo	[30]	1.599-2.894	2.330-4.829

Note: The database in this work only includes the data in the wavelength range from 300-1300 nm.

Table S2. open-circuit voltage losses for perovskite with various bandgaps

Bandgap (eV)	V_{oc}, SQ limit (V)	V_{oc} potential in this work (V)
1.20	0.951	0.836
1.23	0.979	0.907
1.26	1.006	0.946
1.29	1.034	0.974
1.32	1.063	1.003
1.35	1.091	1.031
1.38	1.119	1.059
1.41	1.147	1.087
1.44	1.175	1.115
1.47	1.203	1.143
1.50	1.231	1.171
1.53	1.259	1.199
1.56	1.287	1.227
1.59	1.315	1.255
1.62	1.343	1.283
1.65	1.371	1.311
1.68	1.399	1.325
1.71	1.428	1.322
1.74	1.456	1.319
1.77	1.484	1.315
1.80	1.512	1.314
1.83	1.540	1.315
1.86	1.568	1.317
1.89	1.596	1.319
1.92	1.624	1.320
1.95	1.652	1.318
1.98	1.680	1.312
2.01	1.708	1.304

Table S3. The optimal active layer parameters for 2T configurations.

Albedo (%)	Constrained				Global Optimized			
	PGD	PVSK Thickness	PVSK Eg	CIGS Eg	PGD	PVSK Thickness	PVSK Eg	CIGS Eg
	W/m^2	nm	eV	eV	W/m^2	nm	eV	eV
0	300.89	600	1.65	1.10	311.02	1180	1.74	1.16
10	316.95	600	1.56	1.10	325.50	1200	1.65	1.16
20	327.83	600	1.50	1.10	338.53	1120	1.56	1.15
30	345.21	600	1.41	1.10	352.83	720	1.44	1.13
40	353.44	600	1.35	1.10	368.63	1040	1.44	1.16
50	357.88	600	1.32	1.10	379.31	900	1.38	1.17
60	357.90	600	1.32	1.10	388.20	1140	1.35	1.18
70	357.92	600	1.32	1.10	392.28	1140	1.32	1.20
80	357.94	600	1.32	1.10	392.33	1140	1.32	1.20
90	357.96	600	1.32	1.10	392.38	1140	1.32	1.20
100	357.98	600	1.26	1.10	392.43	1140	1.32	1.20

Table S4. The optimal active layer parameters for 4T configurations

Albedo (%)	Constrained				Global Optimized			
	PGD	PVSK Thickness	PVSK Eg	CIGS Eg	PGD	PVSK Thickness	PVSK Eg	CIGS Eg
	W/cm^2	nm	eV	eV	W/cm^2	nm	eV	eV
0	308.20	600	1.65	1.10	326.90	1200	1.64	1.14
10	328.34	600	1.65	1.10	348.54	1200	1.64	1.14
20	348.41	600	1.65	1.10	370.08	1200	1.69	1.14
30	368.36	600	1.65	1.10	391.50	1200	1.69	1.14
40	388.18	600	1.65	1.10	412.94	1200	1.74	1.15
50	407.84	600	1.65	1.10	434.25	1200	1.74	1.15
60	427.35	600	1.65	1.10	455.41	1200	1.74	1.15
70	446.69	600	1.65	1.10	476.41	1200	1.74	1.15
80	465.85	600	1.65	1.10	497.25	1200	1.74	1.15
90	484.83	600	1.65	1.10	517.91	1200	1.74	1.15
100	503.63	600	1.65	1.10	538.42	1200	1.74	1.16

Table S5. Part of the TMY 3 Data of Miami City.

Date	Time	Zenith Angle (°)	Azimuth Angle (°)	Temperature (°C)
11th June	01:00	130.2	11.9	28.9
11th June	02:00	125.5	28.4	28.9
11th June	03:00	117.7	41.7	26.1
11th June	04:00	107.8	52.2	25.6
11th June	05:00	96.6	60.4	25.0
11th June	06:00	84.3	67.0	25.0
11th June	07:00	71.8	72.6	26.1
11th June	08:00	58.7	77.5	28.3
11th June	09:00	45.5	82.2	30.0
11th June	10:00	32.0	87.2	30.6
11th June	11:00	18.5	94.1	31.1
11th June	12:00	5.4	118.9	31.1
11th June	13:00	9.3	255.1	32.2
11th June	14:00	22.7	268.4	31.7
11th June	15:00	36.2	274.4	31.1
11th June	16:00	49.6	279.2	31.1
11th June	17:00	62.8	284.0	30.6
11th June	18:00	75.7	289.1	30.0
11th June	19:00	88.0	294.9	29.4
11th June	20:00	100.2	302.0	28.9
11th June	21:00	111.0	310.8	28.9
11th June	22:00	120.4	322.1	28.9
11th June	23:00	127.3	336.5	28.9
11th June	24:00	130.8	353.7	28.9

Reference:

1. M. Langenhorst, B. Sautter, R. Schmager, J. Lehr, E. Ahlswede, M. Powalla, U. Lemmer, B. S. Richards and U. W. Paetzold, *Prog. Photovoltaics Res. Appl.*, 2019, **27**, 290-298.
2. M. Jošt, E. Köhnen, A. Al-Ashouri, T. Bertram, Š. Tomšič, A. Magomedov, E. Kasparavicius, T. Kodalle, B. Lipovšek, V. Getautis, R. Schlatmann, C. A. Kaufmann, S. Albrecht and M. Topič, *ACS Energy Lett.*, 2022, **7**, 1298-1307.
3. E. Centurioni, *Appl. Opt.*, 2005, **44**, 7532-7539.
4. R. Schmager, M. Langenhorst, J. Lehr, U. Lemmer, B. S. Richards and U. W. Paetzold, *Opt. Express*, 2019, **27**, A507-A523.
5. M. A. Ruiz-Preciado, F. Gota, P. Fassl, I. M. Hossain, R. Singh, F. Laufer, F. Schackmar, T. Feeney, A. Farag, I. Allegro, H. Hu, S. Gharibzadeh, B. A. Nejand, V. S. Gevaerts, M. Simor, P. J. Bolt and U. W. Paetzold, *ACS Energy Lett.*, 2022, **7**, 2273-2281.
6. A. Bojar, D. Micha, M. Giteau, M. A. Ruiz-Preciado, U. W. Paetzold, M. Simor, V. S. Gevaerts, R. Carron, K. Medjoubi, S. Collin, N. Naghavi, J. F. Guillemoles and P. Schulz, *Journal of Physics-Energy*, 2023, **5**, 035001.
7. S.-C. Yang, T.-Y. Lin, M. Ochoa, H. Lai, R. Kothandaraman, F. Fu, A. N. Tiwari and R. Carron, *Nat. Energy*, 2022, **8**, 40-51.
8. P. Baruch, A. Devos, P. T. Landsberg and J. E. Parrott, *Sol. Energy Mater. Sol. Cells*, 1995, **36**, 201-222.
9. T. Feurer, F. Fu, T. P. Weiss, E. Avancini, J. Löckinger, S. Buecheler and A. N. Tiwari, *Thin Solid Films*, 2019, **670**, 34-40.
10. T. Feurer, R. Carron, G. Torres Sevilla, F. Fu, S. Pisoni, Y. E. Romanyuk, S. Buecheler and A. N. Tiwari, *Adv. Energy Mater.*, 2019, **9**, 1901428.
11. W. Yang, H. Long, X. Sha, J. Sun, Y. Zhao, C. Guo, X. Peng, C. Shou, X. Yang, J. Sheng, Z. Yang, B. Yan and J. Ye, *Adv. Funct. Mater.*, 2022, **32**, 2110698.
12. T. J. Jacobsson, A. Hultqvist, A. García-Fernández, A. Anand, A. Al-Ashouri, A. Hagfeldt, A. Crovetto, A. Abate, A. G. Ricciardulli, A. Vijayan, A. Kulkarni, A. Y. Anderson, B. P. Darwich, B. Yang, B. L. Coles, C. A. R. Perini, C. Rehermann, D. Ramirez, D. Fairen-Jimenez, D. Di Girolamo, D. Jia, E. Avila, E. J. Juarez-Perez, F. Baumann, F. Mathies, G. S. A. González, G. Boschloo, G. Nasti, G. Paramasivam, G. Martínez-Denegri, H. Näsström, H. Michaels, H. Köbler, H. Wu, I. Benesperi, M. I. Dar, I. Bayrak Pehlivan, I. E. Gould, J. N. Vagott, J. Dagar, J. Kettle, J. Yang, J. Li, J. A. Smith, J. Pascual, J. J. Jerónimo-Rendón, J. F. Montoya, J.-P. Correa-Baena, J. Qiu, J. Wang, K. Sveinbjörnsson, K. Hirselandt, K. Dey, K. Frohna, L. Mathies, L. A. Castriotta, M. H. Aldamasy, M. Vasquez-Montoya, M. A. Ruiz-Preciado, M. A. Flatken, M. V. Khenkin, M. Grischek, M. Kedia, M. Saliba, M. Anaya, M. Veldhoen, N. Arora, O. Shargaieva, O. Maus, O. S. Game, O. Yudilevich, P. Fassl, Q. Zhou, R. Betancur, R. Munir, R. Patidar, S. D. Stranks, S. Alam, S. Kar, T. Unold, T. Abzieher, T. Edvinsson, T. W. David, U. W. Paetzold, W. Zia, W. Fu, W. Zuo, V. R. F. Schröder, W. Tress, X. Zhang, Y.-H. Chiang, Z. Iqbal, Z. Xie and E. Unger, *Nat. Energy*, 2022, **7**, 107-115.
13. K. Suchan, T. J. Jacobsson, C. Rehermann, E. L. Unger, T. Kirchartz and C. M. Wolff, *Adv. Energy Mater.*, 2024, **14**, 2303420.
14. R. Gutzler, W. Witte, A. Kanevce, D. Hariskos and S. Paetel, *Prog. Photovoltaics Res. Appl.*, 2023, **31**, 1023-1031.

15. SRRL BMS Outdoor Spectral Data, https://midcdmz.nrel.gov/apps/spectra.pl?BMS).
16. Solar resource maps and GIS data, https://solargis.com/maps-and-gis-data/overview).
17. A. Parisi, R. Pernice, V. Rocca, L. Curcio, S. Stivala, A. C. Cino, G. Cipriani, V. Di Dio, G. R. Galluzzo, R. Miceli and A. C. Busacca, *Int. J. Photoenergy*, 2015, **2015**, 1-9.
18. L. J. Xu, F. Z. Xu, J. Liu, X. C. Zhang, A. S. Subbiah and S. De Wolf, *ACS Energy Lett.*, 2023, **8**, 3114-3121.
19. J. H. Tang, S. Ma, Y. T. Wu, F. T. Pei, Y. Ma, G. Z. Yuan, Z. Y. Zhang, H. P. Zhou, C. Zhu, Y. Jiang, Y. J. Li and Q. Chen, *Sol. RRL*, 2024, **8**, 2300801.
20. L. V. Rodríguez-de Marcos, J. I. Larruquert, J. A. Méndez and J. A. Aznárez, *Opt. Mater. Express*, 2017, **7**, 989-1006.
21. R. J. Moerland and J. P. Hoogenboom, *Optica*, 2016, **3**, 112-117.
22. Y. Jiang, T. Feurer, R. Carron, G. T. Sevilla, T. Moser, S. Pisoni, R. Erni, M. D. Rossell, M. Ochoa, R. Hertwig, A. N. Tiwari and F. Fu, *ACS Nano*, 2020, **14**, 7502-7512.
23. R. E. Treharne, A. Seymour-Pierce, K. Durose, K. Hutchings, S. Roncallo and D. Lane, *Condensed Matter and Materials Physics Conference (Cmmp10)*, 2011, **286**, 012038.
24. O. Aftenieva, J. Brunner, M. Adnan, S. Sarkar, A. Fery, Y. Vaynzof and T. A. F. Konig, *ACS Nano*, 2023, **17**, 2399-2410.
25. P. F. Ndione, Z. Li and K. Zhu, *J. Mater. Chem. C*, 2016, **4**, 7775-7782.
26. K. Dey, B. Roose and S. D. Stranks, *Adv. Mater.*, 2021, **33**, e2102300.
27. C. Stelling, C. R. Singh, M. Karg, T. A. Konig, M. Thelakkat and M. Retsch, *Sci. Rep.*, 2017, **7**, 42530.
28. R. Carron, E. Avancini, T. Feurer, B. Bissig, P. A. Losio, R. Figi, C. Schreiner, M. Burki, E. Bourgeois, Z. Remes, M. Nesladek, S. Buecheler and A. N. Tiwari, *Sci. Technol. Adv. Mater.*, 2018, **19**, 396-410.
29. A. R. Beal and H. P. Hughes, *J. Phys. C: Solid State Phys.*, 1979, **12**, 881-890.
30. W. S. M. Werner, K. Glantschnig and C. Ambrosch-Draxl, *J. Phys. Chem. Ref. Data*, 2009, **38**, 1013-1092.